

# Autonomous Underwater Vehicle Navigation

Paul A. Miller, Jay A. Farrell, *Fellow, IEEE*, Yuanyuan Zhao, and Vladimir Djapic

**Abstract**—This paper considers the vehicle navigation problem for an autonomous underwater vehicle (AUV) with six degrees of freedom. We approach this problem using an error state formulation of the Kalman filter. Integration of the vehicle's high-rate inertial measurement unit's (IMU's) accelerometers and gyros allow time propagation while other sensors provide measurement corrections. The low-rate aiding sensors include a Doppler velocity log (DVL), an acoustic long baseline (LBL) system that provides round-trip travel times from known locations, a pressure sensor for aiding depth, and an attitude sensor. Measurements correct the filter independently as they arrive, and as such, the filter is not dependent on the arrival of any particular measurement. We propose novel tightly coupled techniques for the incorporation of the LBL and DVL measurements. In particular, the LBL correction properly accounts for the error state throughout the measurement cycle via the state transition matrix. Alternate tightly coupled approaches ignore the error state, utilizing only the navigation state to account for the physical latencies in the measurement cycle. These approaches account for neither the uncertainty of vehicle trajectory between interrogation and reply, nor the error state at interrogation. The navigation system also estimates critical sensor calibration parameters to improve performance. The result is a robust navigation system. Simulation and experimental results are provided.

**Index Terms**—Acoustic long baseline (LBL) aiding, Doppler aiding, inertial navigation, Kalman filter, underwater vehicles.

## I. INTRODUCTION

WITH the emergence of inspection-class autonomous underwater vehicles (AUVs), navigation and navigational accuracy are becoming increasingly important. Without an operator in the loop, the vehicle itself must use sensors to determine its location, orientation, motion, and interpret its surroundings such that it can maneuver through complex environments. Autonomous inspection vehicles are often required to localize targets within submeter accuracy for later analysis or prosecution. Their navigation routines rely on unique acoustic sensors to provide feedback. It is the integration of these sensors with an inertial navigation system that presents interesting challenges. Survey papers [1] and [2] provide a detailed assessment

of sensor technology and algorithms for underwater vehicle navigation. Here, we derive and utilize methods suitable for an error state formulation of the Kalman filter [3]–[6] to provide an optimal and robust solution to the vehicle navigation problem. This paper concentrates on the application of the Kalman filter and development of the model and filter algorithms. It does not attempt to justify the Kalman filter itself or to make comparisons to alternatives to the Kalman filter. This paper aims to provide sufficient information for others to replicate results.

The vehicle of interest contains a unique suite of on-board sensors that provide information related to the vehicle's navigation state. The primary sensor is an inertial measurement platform [Crossbow VG-700CA fiber-optic gyro (FOG)] that measures accelerations and angular rates in three dimensions. We choose to utilize this sensor in a strapdown configuration. This low-cost sensor is reliable, but due to noise and unknown biases, it alone cannot provide sufficient navigational accuracy. Other sensors provide additional feedback. A Doppler velocity log (DVL; RD Instruments 1200-kHz Workhorse Navigator) provides velocities along four beam directions via acoustic Doppler measurements. An acoustic long baseline (LBL) system (Desert Star Aqua Map LBL) measures round-trip travel times between a vehicle transceiver and four remote transponders. An attitude and pressure sensor complete the navigation suite. The attitude sensor (Honeywell HMR3000) provides orientation measurements, while the pressure sensor (Desert Star SSP-1 100 psi) provides a sense of vehicle depth. We assume that the platform-frame sensor locations are known exactly and that all measurements, except for the LBL, have negligible measurement latencies. Delay is inherent in the LBL system, and methods to address that delay to enhance navigation accuracy are a major contribution of this paper. Fig. 1 illustrates the general sensor configuration. Performance specifications are provided as each sensor is discussed. Note that the vehicle and sensor suite were of opportunity, and in no way, were they optimized for our particular application.

The literature contains numerous references to the use of DVL sensors for underwater vehicle navigation. Combined with an attitude reference, this highly regarded sensor can provide sufficient navigational accuracy for many applications. However, some applications stress this sensor by operating in close proximity to the seafloor or other reference surfaces, or by operating at an extreme tilt angle where one or more DVL beams do not provide a reflection. In such situations, the sensor may fail to maintain *bottom lock*. Bottom lock refers to the condition when a sufficient number of beam measurements are available to relate the measured beam velocities to instrument frame velocities via geometry transformation [7]. To our knowledge, all DVL-aided applications utilize an instrument

Manuscript received March 12, 2009; revised March 15, 2010; accepted May 14, 2010. Date of publication August 12, 2010; date of current version September 01, 2010.

**Associate Editor:** D. Stilwell.

P. A. Miller was with the SPAWAR Systems Center San Diego, San Diego, CA 92152-5001 USA. He is now with Mine Safety Appliances (MSA), Cranberry Twp., PA 16066-5296 USA (e-mail: pmiller79@gmail.com).

J. A. Farrell is with the Department of Electrical Engineering, University of California Riverside, Riverside, CA 92502 USA.

Y. Zhao was with the University of California Riverside, Riverside, CA 92502 USA. She is now with the Servo Department, Western Digital Corporation, Lake Forest, CA 92630-7741 USA.

V. Djapic is with the NATO Undersea Research Centre (NURC), La Spezia 19126, Italy.

Digital Object Identifier 10.1109/JOE.2010.2052691

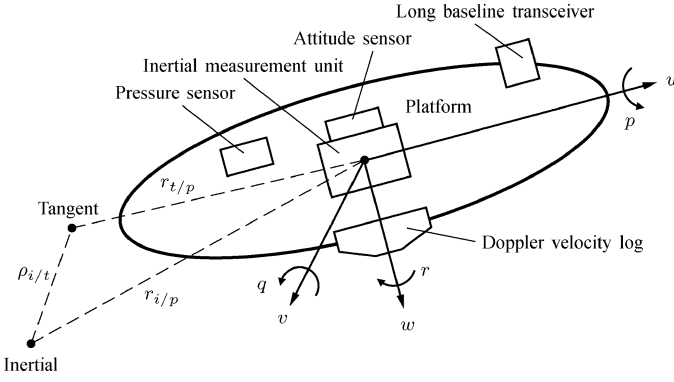


Fig. 1. Vehicle sensor configuration. All sensors remain fixed within the platform frame.

frame or another derived coordinate frame to correct the filter [8]–[10]. In Section III-F2, we propose a tightly coupled aiding algorithm for the DVL measurement correction. This approach does not require bottom lock and allows individual validation and characterization of the DVL beam measurements.

The acoustic LBL system measures round-trip travel times between the vehicle transceiver and remote transponders at known locations. The LBL transponder on the AUV emits a common interrogate ping, then listens for sequential replies from four baseline stations. The entire measurement cycle takes almost 2 s for operating areas less than  $350 \times 350 \text{ m}^2$ . If the vehicle were to remain stationary during this time, the ranges between the vehicle and each baseline station, and hence the vehicle position, could be easily estimated from the respective round-trip times. When the vehicle is moving, the ranges are less obvious as the measurements depend on the vehicle transmit and receive positions, and as such, trilateration solutions produce erroneous results. Due to the inherent physical latencies, a tightly coupled aiding approach is desirable. Proposed approaches [9], [11]–[13] propagate the navigation state backwards in time to estimate the time or range of each segment. In Section III-F3, we propose a method that uses the known relationship between the error state at the interrogation and reception instants.

We organize this paper as follows. Section II develops the continuous-time model for this system, while Section III formulates the corresponding navigation equations. In Section IV, we choose several interesting scenarios to analyze critical aspects of our approach. The final two sections include experimental results and a conclusion.

## II. MODEL DERIVATION

Our navigation model uses well-understood kinematic relationships for rigid body motion, where the inertial frame is coincident with the Earth center. We assume a fixed tangent frame of reference with a north–east–down coordinate system. For completeness, to clarify notation [14], and to clearly state assumptions, we present a brief derivation herein. Let vector  $\rho_{i/t}$  describe the position of the tangent plane origin relative to the inertial frame origin, and vector  $r_{t/p}$  describe the position of the platform relative to the tangent plane origin. The position

of the platform with respect to the inertial frame is therefore  $r_{i/p} = \rho_{i/t} + r_{t/p}$ . Using a superscript to indicate the frame of reference, we represent the position and velocity as

$$\begin{aligned} r_{i/p}^i &= \rho_{i/t}^i + R_t^i r_{t/p}^t \\ \dot{r}_{i/p}^i &= \dot{\rho}_{i/t}^i + R_t^i [\Omega_{i/t}^t r_{t/p}^t + \dot{r}_{t/p}^t] \end{aligned} \quad (1)$$

in the inertial frame. For compactness, we represent the Earth rate cross product  $\omega_{i/t}^t \times r_{t/p}^t$  as  $\Omega_{i/t}^t r_{t/p}^t$ , where  $\Omega_{i/t}^t = [\omega_{i/t}^t \times]$  is the skew symmetric matrix cross product form<sup>1</sup> of the vector  $\omega_{i/t}^t$ . Earth rate  $\omega_{i/t}^t$  represents the rotation rate of tangent frame  $t$  with respect to inertial frame  $i$ , and represented in the tangent frame. Differentiating (1) with respect to time to obtain  $\ddot{r}_{i/p}^i$ , and then solving for the acceleration of the platform relative to the tangent frame  $\ddot{r}_{t/p}^t$  yields

$$\begin{aligned} \ddot{r}_{t/p}^t &= \ddot{r}_{i/p}^i - \ddot{\rho}_{i/t}^i - \Omega_{i/t}^t \Omega_{i/t}^t r_{t/p}^t - 2\Omega_{i/t}^t \dot{r}_{t/p}^t - \dot{\Omega}_{i/t}^t r_{t/p}^t \\ &= (f_{i/p}^t + G_{i/p}^t) - \ddot{\rho}_{i/t}^i - \Omega_{i/t}^t \Omega_{i/t}^t r_{t/p}^t - 2\Omega_{i/t}^t \dot{r}_{t/p}^t - \dot{\Omega}_{i/t}^t r_{t/p}^t \\ &= f_{i/p}^t + (G_{i/p}^t - \Omega_{i/t}^t \Omega_{i/t}^t r_{t/p}^t) - \ddot{\rho}_{i/t}^i - 2\Omega_{i/t}^t \dot{r}_{t/p}^t - \dot{\Omega}_{i/t}^t r_{t/p}^t \\ &= f_{i/p}^t + g_{i/p}^t - 2\Omega_{i/t}^t \dot{r}_{t/p}^t \end{aligned} \quad (2)$$

where we have substituted using the definition of the specific force vector  $f_{i/p}^t = \ddot{r}_{i/p}^i - G_{i/p}^t$  [14]. The position-dependent gravity vector (i.e., local or plumb bob gravity) is the gravitational force plus centripetal acceleration, or  $g_{i/p}^t = G_{i/p}^t - \Omega_{i/t}^t \Omega_{i/t}^t r_{t/p}^t$ . We assume that the tangent frame origin is fixed such that  $\ddot{\rho}_{i/t}^i = 0$  and  $\omega_{i/t}^t = \omega_{i/e}^t$ , and the Earth rotational rate is constant,  $\dot{\omega}_{i/e}^t = 0$ . The Earth rotational rate in tangent frame is  $\omega_{i/e}^t = \omega_{i/e}^t [\cos \bar{\phi}, 0, -\sin \bar{\phi}]^T$ , where  $\bar{\phi}$  is the vehicle latitude.

In this paper, the navigation system represents and computes the Earth relative velocity in platform frame  $v_{t/p}^p$ . Because  $v_{t/p}^p = \dot{r}_{t/p}^p$  and  $\dot{r}_{t/p}^p = R_t^p \dot{r}_{t/p}^t$ , using (2), we obtain

$$\begin{aligned} \dot{r}_{t/p}^p &= R_t^p \dot{r}_{t/p}^t + R_t^p \ddot{r}_{t/p}^t \\ &= (-\Omega_{i/t}^t R_t^p) R_t^p \dot{r}_{t/p}^t + R_t^p (f_{i/p}^t + g_{i/p}^t - 2\Omega_{i/t}^t \dot{r}_{t/p}^t) \\ \dot{v}_{t/p}^p &= f_{i/p}^p + R_t^p g_{i/p}^t - R_t^p \Omega_{i/t}^t R_t^p v_{t/p}^p - \Omega_{i/p}^p v_{t/p}^p. \end{aligned} \quad (3)$$

For brevity, we will drop subscripts from the local gravity vector hereafter.

We use a Euler attitude representation to describe vehicle orientation, where a Euler 3-2-1 rotation sequence [15] defines the relationship between tangent and platform frames. The combined rotation sequence from tangent frame  $t$  to platform frame  $p$  is

$$R_t^p = R_1(\phi) R_2(\theta) R_3(\psi)$$

with inverse  $R_p^t = (R_t^p)^{-1} = (R_t^p)^T$ .

It is important to note that each Euler angle describes a rotation about an axis in a distinct frame. We exploit the known relationships between the intermediate frames to relate the Euler attitude rates  $(\dot{\phi}, \dot{\theta}, \dot{\psi})$  to the angular rates in the platform frame  $\omega_{t/p}^p$  in Section III-F1. If we denote the frame that results from the  $\psi$  rotation as frame 1 with coordinate axes in directions

<sup>1</sup>See [4, p.57 eq. (2.74)].

$(\hat{i}_1, \hat{j}_1, \hat{k}_1)$  and the frame that results from the subsequent  $\theta$  rotation as frame 2 with coordinate axes in directions  $(\hat{i}_2, \hat{j}_2, \hat{k}_2)$ , then

$$\begin{aligned}\omega_{t/p}^p &= \omega_{t/1}^p + \omega_{1/2}^p + \omega_{2/p}^p \\ &= R_1(\phi)R_2(\theta)\dot{\psi}\hat{k}_1 + R_1(\phi)\dot{\theta}\hat{j}_2 + \dot{\phi}\hat{i}_p.\end{aligned}$$

In matrix form, the Euler and platform angular rates are related by  $\omega_{t/p}^p = \Omega\dot{\Theta}$ , where  $\dot{\Theta} = [\dot{\phi}, \dot{\theta}, \dot{\psi}]^\top$ . More importantly, for integration of the Euler angles  $\Theta$  using the gyro measurements, we have

$$\dot{\Theta} = \Omega^{-1}\omega_{t/p}^p. \quad (4)$$

Note that  $\Omega^{-1}$  approaches a singularity as  $\theta \rightarrow \pm\pi/2$ . It is assumed that the vehicle will not operate near this singularity. If operation near  $\pm\pi/2$  is desired, then an alternative attitude representation [16], [17], such as quaternions [18], [19], would remove this singularity. Given (3), (4), and that  $\omega_{t/p} = \omega_{i/p} - \omega_{i/t}$ , the continuous-time kinematic model is

$$\left. \begin{aligned}\dot{r}_{t/p}^t &= R_p^t v_{t/p}^p \\ \dot{\Theta} &= \Omega^{-1}(\omega_{i/p}^p - R_t^p \omega_{i/e}^t) \\ \dot{v}_{t/p}^p &= f_{i/p}^p + R_t^p g^t - R_t^p \Omega_{i/e}^t R_p^t v_{t/p}^p - \Omega_{i/p}^p v_{t/p}^p\end{aligned} \right\}. \quad (5)$$

The next section utilizes this model, along with bias and measurement models, to propagate the system through time and formulate measurement predictions.

### III. NAVIGATION

In the following sections, we formulate dynamic equations for the error state and apply the Kalman filter to estimate the error state. The formulation of the time propagation of the system state revolves around the system's inertial measurement unit (IMU), and as such, we describe this sensor first in Section III-A. Section III-B defines the augmented system equations. These equations model the true system, while Section III-C defines the mechanization equations that propagate the navigation state vector  $\hat{x}$ . The difference between the actual and mechanized systems is the error state system. A continuous-time model for the dynamics of error state system is described in Section III-D. Section III-E derives equivalent discrete-time error dynamic equations that are necessary for implementation of the Kalman filter. Section III-F then applies the Kalman filter measurement correction equations to the aiding sensors.

#### A. Inertial Measurement Unit

The IMU is the primary high-rate sensor. It measures the specific force vector via accelerometers and angular rates via FOGs. The IMU effective measurement point defines the origin of the platform frame. The IMU also provides an accurate time measurement since the last IMU update. This delta time measurement is useful for precise integration, described in Section III-E. We expect this sensor to provide continuous updates without interruption.

The specific force and angular rate measurement vectors of the accelerometer and gyro  $y_a$  and  $y_g$ , respectively, are modeled by

$$y_a = f_{i/p}^p + b_a + n_a \quad (6a)$$

$$y_g = \omega_{i/p}^p + b_g + n_g \quad (6b)$$

where  $(b_a, n_a)$  and  $(b_g, n_g)$  are bias and measurement noise vectors. Noise vectors  $n_a$  and  $n_g$  are distributed according to  $N(0, \sigma_a^2 I)$  and  $N(0, \sigma_g^2 I)$ , respectively, and are assumed to be white noise processes [3]. The specific force vector and angular rate estimates are computed as

$$\hat{f}_{i/p}^p = y_a - \hat{b}_a \quad (7a)$$

$$\hat{\omega}_{i/p}^p = y_g - \hat{b}_g. \quad (7b)$$

Bias vectors  $b_a$  and  $b_g$  are modeled as random constants plus random walks, where

$$\dot{b}_a = \omega_a, \quad \dot{\hat{b}}_a = 0 \quad (8a)$$

$$\dot{b}_g = \omega_g, \quad \dot{\hat{b}}_g = 0. \quad (8b)$$

The driving noise vectors  $\omega_a$  and  $\omega_g$  are distributed according to  $N(0, \sigma_{ba}^2 I)$  and  $N(0, \sigma_{bg}^2 I)$ , respectively. We assume IMU noise parameters

- $\sigma_a \approx 0.01 \text{ m/(s } \sqrt{\text{s}})$ ;
- $\sigma_{ba} \approx 1 \times 10^{-4} \text{ m/(s}^2 \sqrt{\text{s}})$ ;
- $\sigma_g \approx 0.11636 \times 10^{-3} \text{ rad/}\sqrt{\text{s}}$ ;
- $\sigma_{bg} \approx 1 \times 10^{-6} \text{ rad/(s } \sqrt{\text{s}})$ .

The update rate is 150 Hz.

#### B. Augmented System Equations

Augmenting our continuous-time model, in (5), with the models for the unknown parameters in (8a) and (8b), yields the system state vector

$$x = [(r_{t/p}^t)^\top \quad \Theta^\top \quad (v_{t/p}^p)^\top \quad b_a^\top \quad b_g^\top \quad c]^\top.$$

The additional parameter  $c$  represents our estimate for the speed of sound in seawater. We model  $c$  as a random constant plus random walk with driving noise  $\omega_c \sim N(0, \sigma_c^2)$ , where  $\sigma_c \approx 0.1 \text{ m/(s } \sqrt{\text{s}})$ . This estimate is necessary to calculate round-trip distances from travel times for the LBL system, described in Section III-F3. The process noise input vector is

$$u = [n_a^\top \quad n_g^\top \quad \omega_a^\top \quad \omega_g^\top \quad \omega_c]^\top \quad (9)$$

where all quantities are mutually uncorrelated, Gaussian, white noise vectors. Therefore, the augmented true system equations are as shown in (10) at the bottom of the next page, where we have substituted for  $f_{i/p}^p$  and  $\omega_{t/p}^p$  with (6a) and (6b), respectively, in preparation for the development of the error state equations in Section III-D.

#### C. Mechanization Equations

Based upon (10), the estimate of the system state vector

$$\hat{x} = [(\hat{r}_{t/p}^t)^\top \quad \hat{\Theta}^\top \quad (\hat{v}_{t/p}^p)^\top \quad \hat{b}_a^\top \quad \hat{b}_g^\top \quad \hat{c}]^\top$$

is propagated through time by integration of the IMU measurements using mechanization equations

$$\left. \begin{aligned} \dot{\hat{r}}_{t/p}^t &= \hat{R}_p^t \hat{v}_{t/p}^p \\ \dot{\hat{\Theta}} &= \hat{\Omega}^{-1}(y_g - \hat{b}_g - \hat{R}_t^p \hat{\omega}_{i/e}^t) \\ \dot{\hat{v}}_{t/p}^p &= (y_a - \hat{b}_a) + \hat{R}_t^p \hat{g}^t - \hat{R}_t^p \hat{\Omega}_{i/e}^t \hat{R}_t^p \hat{v}_{t/p}^p - (y_g - \hat{b}_g) \times \hat{v}_{t/p}^p \\ \dot{\hat{b}}_a &= 0 \\ \dot{\hat{b}}_g &= 0 \\ \dot{\hat{c}} &= 0 \end{aligned} \right\} \quad (11)$$

where the gravity vector  $\hat{g}^t(\hat{r}_{t/p}^t)$  and tangent frame rotation rate  $\hat{\Omega}_{i/e}^t(\hat{r}_{t/p}^t)$  are functions of the estimated position.

#### D. Error State Equations

The error state equations represent the expected value of the error between the true system and its estimate  $\delta \dot{x} = \dot{x} - \dot{\hat{x}}$ . To compute the transformation error between two rotation matrices, we define a small-angle transformation as  $\hat{R}_p^t = (I - [\delta \rho \times])R_p^t$ , where  $(I - [\delta \rho \times])$  represents a small-angle transformation from the true tangent frame to the computed tangent frame [20]. The quantity  $\delta \rho$  represents the small-angle error vector between the true and computed frames. The error state vector is then

$$\delta x = [(\delta r_{t/p}^t)^\top \quad \delta \rho^\top \quad (\delta v_{t/p}^p)^\top \quad \delta b_a^\top \quad \delta b_g^\top \quad \delta c]^\top \quad (12)$$

where  $\delta \rho$  replaces  $\delta \Theta$ . The following relations are useful in the subsequent analysis:

$$\hat{R}_p^t = (I - [\delta \rho \times])R_p^t \quad (13a)$$

$$R_p^t = (I + [\delta \rho \times])\hat{R}_p^t \quad (13b)$$

$$\hat{R}_t^p = R_t^p(I + [\delta \rho \times]) \quad (13c)$$

$$R_t^p = \hat{R}_t^p(I - [\delta \rho \times]). \quad (13d)$$

Using the small-angle relationships, we compute the error state equations for each state. The tangent position error is

$$\begin{aligned} \delta \hat{r}_{t/p}^t &= \dot{\hat{r}}_{t/p}^t - \dot{r}_{t/p}^t = \hat{R}_p^t \hat{v}_{t/p}^p - \hat{R}_p^t \hat{v}_{t/p}^p \\ &= (\hat{R}_p^t + [\delta \rho \times] \hat{R}_p^t)(\delta v_{t/p}^p + \hat{v}_{t/p}^p) - \hat{R}_p^t \hat{v}_{t/p}^p \\ &= \hat{R}_p^t \delta v_{t/p}^p + [\delta \rho \times] \hat{R}_p^t \delta v_{t/p}^p + [\delta \rho \times] \hat{R}_p^t \hat{v}_{t/p}^p \\ &\approx \hat{R}_p^t \delta v_{t/p}^p - [\hat{R}_p^t \hat{v}_{t/p}^p \times] \delta \rho \end{aligned} \quad (14)$$

where we used (13b) and the fact that  $[a \times]b = -[b \times]a$  to manipulate the terms such that the error state coefficients can be represented in matrix form. Note the substitution for  $\hat{v}_{t/p}^p$ . We do not replace the true state with its estimate. For example,  $v_{t/p}^p = \hat{v}_{t/p}^p + \delta v_{t/p}^p$ . It is incorrect to assume that  $v_{t/p}^p$  is equivalent to  $\hat{v}_{t/p}^p$ . Approximations occur when second-order terms are dropped. In this case, second-order term  $[\delta \rho \times] \hat{R}_p^t \delta v_{t/p}^p$  is dropped in the final linearized result.

To determine the error state model for  $\delta \dot{\rho}$  [14], differentiate the rotation matrix error  $\delta R_p^t = [\delta \rho \times] R_p^t$

$$\delta \dot{R}_p^t = [\delta \dot{\rho} \times] R_p^t + [\delta \rho \times] \dot{R}_p^t = [\delta \dot{\rho} \times] R_p^t + [\delta \rho \times] (R_p^t \Omega_{t/p}^p)$$

and solve for  $[\delta \dot{\rho} \times]$

$$\begin{aligned} [\delta \dot{\rho} \times] &= (\dot{R}_p^t - \dot{\hat{R}}_p^t) R_p^t - [\delta \rho \times] R_p^t \Omega_{t/p}^p R_p^t \\ &= (R_p^t \Omega_{t/p}^p - \hat{R}_p^t \hat{\Omega}_{t/p}^p) R_p^t - [\delta \rho \times] \Omega_{t/p}^p \\ &= \Omega_{t/p}^t - \hat{R}_p^t \hat{\Omega}_{t/p}^p \hat{R}_p^t (I - [\delta \rho \times]) - [\delta \rho \times] (\hat{\Omega}_{t/p}^t + \delta \Omega_{t/p}^t) \\ &\approx \Omega_{t/p}^t - \hat{\Omega}_{t/p}^t + \hat{\Omega}_{t/p}^t [\delta \rho \times] - [\delta \rho \times] \hat{\Omega}_{t/p}^t. \end{aligned} \quad (15)$$

The second-order term  $[\delta \rho \times] \delta \Omega_{t/p}^t$  is dropped in (15). Equivalently, expression (15) written in vector form is

$$\begin{aligned} \delta \dot{\rho} &= \omega_{t/p}^t - \hat{\omega}_{t/p}^t + \hat{\omega}_{t/p}^t \times \delta \rho \\ &= R_p^t \omega_{i/p}^p - \hat{R}_p^t \hat{\omega}_{i/p}^p - \delta \omega_{i/t}^t + (\hat{R}_p^t \hat{\omega}_{i/p}^p - \hat{\omega}_{i/t}^t) \times \delta \rho \\ &= \hat{R}_p^t \delta \omega_{i/p}^p + [\delta \rho \times] \hat{R}_p^t \delta \omega_{i/p}^p - \delta \omega_{i/t}^t - \hat{\omega}_{i/t}^t \times \delta \rho \\ &\approx \hat{R}_p^t (-\delta b_g - n_g) - \delta \omega_{i/t}^t - \hat{\omega}_{i/t}^t \times \delta \rho \end{aligned} \quad (16)$$

where  $\delta \omega_{i/t}^t = \{-\omega_{i/e} [\sin \bar{\phi}, 0, \cos \bar{\phi}]^\top \partial \bar{\phi} / \partial r_{t/p}^t\} \delta r_{t/p}^t$  and  $\bar{\phi}$  is the vehicle latitude.

The platform velocity error is

$$\begin{aligned} \delta \dot{v}_{t/p}^p &= \dot{v}_{t/p}^p - \dot{\hat{v}}_{t/p}^p \\ &\approx \hat{R}_t^p \left\{ [\hat{g}^t \times] + \hat{\omega}_{i/e}^t (\hat{R}_p^t \hat{v}_{t/p}^p)^\top - (\hat{\omega}_{i/e}^t \cdot \hat{R}_p^t \hat{v}_{t/p}^p) I \right\} \delta \rho \\ &\quad - \left\{ [(y_g - \hat{b}_g) \times] + \hat{R}_t^p \hat{\Omega}_{i/e}^p \hat{R}_t^p \right\} \delta v_{t/p}^p - \delta b_a - n_a \\ &\quad - [\hat{v}_{t/p}^p \times] \delta b_g - [\hat{v}_{t/p}^p \times] n_g + \hat{R}_t^p \delta g^t + \hat{R}_t^p [\hat{R}_p^t \hat{v}_{t/p}^p \times] \delta \omega_{i/e}^t \end{aligned} \quad (17)$$

where second-order terms have been dropped.

$$\left. \begin{aligned} \dot{\hat{r}}_{t/p}^t &= R_p^t v_{t/p}^p \\ \dot{\hat{\Theta}} &= \Omega^{-1}(y_g - b_g - n_g - R_t^p \omega_{i/e}^t) \\ \dot{v}_{t/p}^p &= (y_a - b_a - n_a) + R_t^p g^t - R_t^p \Omega_{i/e}^p R_p^t v_{t/p}^p - (y_g - b_g - n_g) \times v_{t/p}^p \\ \dot{b}_a &= \omega_a \\ \dot{b}_g &= \omega_g \\ \dot{c} &= \omega_c \end{aligned} \right\} \quad (10)$$

Remaining error expressions for  $\delta b_a$ ,  $\delta b_g$ , and  $\delta c$  are trivial and, as such, their derivation is not shown. The resulting continuous-time error state system is

$$\delta \dot{x}(t) = F(t)\delta x(t) + G(t)u(t) \quad (18)$$

where  $u$  is defined in (9)

$$F(t) = \begin{bmatrix} 0 & -[\hat{R}_p^t \hat{v}_{t/p}^p \times] & \hat{R}_p^t & 0 & 0 & 0 \\ F_{21} & -\hat{\Omega}_{i/e}^t & 0 & 0 & -\hat{R}_p^t & 0 \\ F_{31} & F_{32} & F_{33} & -I & -[\hat{v}_{t/p}^p \times] & 0 \\ 0 & 0 & 0 & 0 & 0 & 0 \\ 0 & 0 & 0 & 0 & 0 & 0 \\ 0 & 0 & 0 & 0 & 0 & 0 \end{bmatrix}$$

$$F_{21} = \frac{\partial \omega_{i/t}^t}{\partial r_{t/p}^t}$$

$$F_{31} = \hat{R}_p^t \left\{ \frac{\partial g^t}{\partial r_{t/p}^t} + [\hat{R}_p^t \hat{v}_{t/p}^p \times] \frac{\partial \omega_{i/e}^t}{\partial r_{t/p}^t} \right\}$$

$$F_{32} = \hat{R}_p^t \left\{ [\hat{g}^t \times] + \hat{\omega}_{i/e}^t (\hat{R}_p^t \hat{v}_{t/p}^p)^\top - (\hat{\omega}_{i/e}^t \cdot \hat{R}_p^t \hat{v}_{t/p}^p) I \right\}$$

$$F_{33} = -[(y_g - \hat{b}_g) \times] - \hat{R}_p^t \hat{\Omega}_{i/e}^t \hat{R}_p^t$$

and

$$G(t) = \begin{bmatrix} 0 & 0 & 0 & 0 & 0 \\ 0 & -\hat{R}_p^t & 0 & 0 & 0 \\ -I & -[\hat{v}_{t/p}^p \times] & 0 & 0 & 0 \\ 0 & 0 & I & 0 & 0 \\ 0 & 0 & 0 & I & 0 \\ 0 & 0 & 0 & 0 & I \end{bmatrix}.$$

Due to the relatively small operating area, we assume that  $F_{21}$  and  $F_{31}$  are approximately zero. Note that the error state vector contains  $\delta \rho$ , while the navigation state contains  $\Theta$ . The measurement correction routines in Section III-F will account for the use of  $\delta \rho$  to correct  $\Theta$ .

### E. Time Propagation

The time propagation routine propagates the navigation state, error state, and error state covariance through time. Fig. 2 illustrates this process. For each measurement update from the IMU, the time propagation routine computes the continuous-time model parameter  $F(t)$ ,  $G(t)$ , and  $Q$ ; computes the discrete-time model parameters  $\Phi$  and  $Q_d$ ; propagates the navigation state  $\hat{x}$ ; and propagates the error state  $\delta x$  and its covariance matrix  $P$ . We assume  $Q = \text{diag}(\sigma_a^2 I, \sigma_b^2 I, \sigma_{ba}^2 I, \sigma_{bg}^2 I, \sigma_c^2)$ . To compute the equivalent<sup>2</sup> discrete-time system, we compute the matrix exponential

$$\Upsilon_k = \exp \left( \begin{bmatrix} -F & GQG^\top \\ 0 & F^\top \end{bmatrix} \Delta t \right)$$

<sup>2</sup>Although matrices  $F$  and  $G$  are time varying, their time variation is small over the IMU sampling time interval  $\Delta t$ ; therefore, the equivalence is not exact and  $\Phi$  and  $Q_d$  are time varying. The subscripts  $k$  to denote the time variation are dropped to simplify the notation.

using algorithms from [21] at each iteration. Quantity  $\Delta t$  is the integration period from the IMU. The result is

$$\Upsilon_k = \begin{bmatrix} -D & \Phi^{-1} Q_d \\ 0 & \Phi^\top \end{bmatrix} \quad (19)$$

where matrices  $\Phi$  and  $Q_d$  parameterize the discrete-time system at time  $k$  [4]. Matrix  $\Phi(k+1, k)$  propagates the error state  $\delta x_k^-$  and covariance  $P_k^-$ , where  $P_k^- = E\langle \delta x_k^- \delta x_k^{-\top} \rangle$ , from time  $k$  to  $k+1$  according to

$$\delta x_{k+1}^- = \Phi_k \delta x_k^- \quad (20)$$

$$P_{k+1}^- = \Phi_k P_k^- \Phi_k^\top + Q_d \quad (21)$$

respectively. Matrix  $Q_d(k)$  quantifies the discrete-time process noise distribution matrix at time  $k$ , and  $D$  is a nonzero dummy matrix. Given  $\Upsilon$ , matrices  $\Phi(k+1, k)$  and  $Q_d(k)$  are trivially solved from its submatrices. Note that when propagating  $P_k$  numerically, it is necessary to occasionally correct symmetry errors using  $P_k$  replaced by  $(1/2)(P_k + P_k^\top)$  and limit the diagonal elements from becoming exactly zero. We perform this procedure at 1 Hz.

We propagate the navigation state estimate  $\hat{x}^-$  using a predictor-corrector integration algorithm [22]

$$\left. \begin{aligned} \hat{x}_{k+1}^p &= \hat{x}_k^- + f(\hat{x}_k^-, y_k) \Delta t \\ \hat{x}_{k+1}^c &= \hat{x}_k^- + f(\hat{x}_{k+1}^p, y_k) \Delta t \\ \hat{x}_{k+1}^- &= \frac{1}{2}(\hat{x}_{k+1}^p + \hat{x}_{k+1}^c) \end{aligned} \right\} \quad (22)$$

where  $y_k = [y_a(k), y_g(k)]^\top$ , then correct the resulting attitude angles to lie on interval  $[-\pi, \pi)$ . Function  $f(x, y)$  is the continuous-time mechanization described in (11). An alternate implementation might utilize coning and sculling integration algorithms to improve performance. For a comprehensive study of integration algorithms, consult [23] and [24].

### F. Measurement Corrections

In this section, we use the terms *sensor* and *measurement* to refer to all sensors other than the IMU. These aiding sensors are discussed in Sections III-F1–III-F4. Each sensor runs independent of the next, with its own update rate and performance characteristics. Thus, measurement corrections are asynchronous. As a measurement arrives, it is evaluated and then incorporated into the error state estimate. If a measurement does not arrive, no calculations are necessary. The algorithm does not wait for or expect measurements to arrive in a predictable fashion; the error state covariance and navigation state will propagate according to (21) and (22), respectively, via the IMU data, with or without measurement corrections. Fig. 3 illustrates the measurement correction routine.

Measurements are evaluated with several sanity checks. One such check verifies that the measurement lies within three standard deviations of its estimate,  $(\delta y_k - H_k \delta x_k^-)^2 < 9(H_k P_k^- H_k^\top + R_k)$ , where  $\delta y_k$  is the measurement residual and matrix  $(H_k P_k^- H_k^\top + R_k)$  represents the measurement covariance. Additional logic is necessary to help ensure that this algorithm does not disregard valid measurements, especially

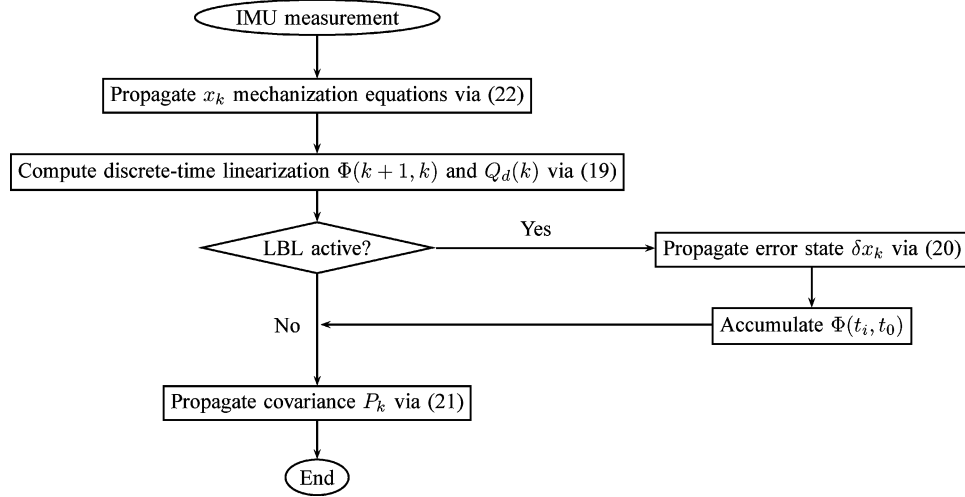


Fig. 2. Time propagation routine. Reception of an IMU measurement triggers propagation of the navigation state  $x_k$ , computation of the discrete-time linearization, and propagation of the error state and its covariance. Accumulation of state transition matrix  $\Phi(t_i, t_0)$  is necessary for the LBL correction discussed in Section III-F3.

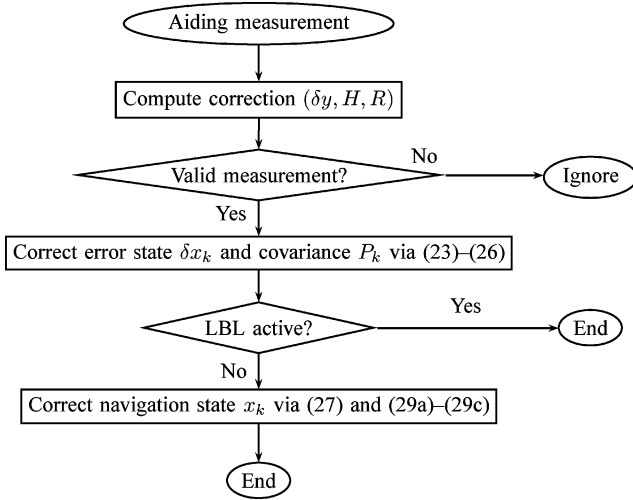


Fig. 3. Measurement correction routine. Reception of an aiding measurement triggers computation of correction  $(\delta y, H, R)$ , measurement validation, and an error state and covariance correction. During an LBL measurement cycle, as discussed in Section III-F3, the error state  $\delta x$  propagates separate from navigation state  $x$ . When the LBL measurement cycle is not active,  $\delta x_k^+$  is incorporated into  $x_k^+$  immediately.

upon initialization. For example, one could require that the diagonal elements of  $P_k^-$  are sufficiently small before validating measurements. Another technique is to monitor running averages of the measurement residuals, where the expected value is zero. If the running average exceeds some threshold, then all measurements should be assumed valid. Valid measurements correct the error state estimate  $\delta x_k$  and covariance  $P_k$  using

$$K_k = P_k^- H_k^\top (H_k P_k^- H_k^\top + R_k)^{-1} \quad (23)$$

$$\delta y_k = y_k - h(\hat{x}_k^-) \quad (24)$$

$$\delta x_k^+ = \delta x_k^- + K_k (\delta y_k - H_k \delta x_k^-) \quad (25)$$

$$P_k^+ = (I - K_k H_k) P_k^- \quad (26)$$

where (23) computes the optimal Kalman gain, (24) computes the measurement residual, (25) corrects the error state estimate, and (26) updates the error state covariance matrix. Circular (i.e., angular) measurements should correct the innovation  $(\delta y_k - H \delta x_k^-)$  to lie on interval  $[-\pi, \pi)$ . Superscript  $-$  indicates the *a priori* state or covariance at time  $k$  immediately before the measurement correction. Superscript  $+$  indicates the *a posteriori* state or covariance at time  $k$  immediately after the measurement correction.

Recognizing the difference between the error state  $\delta x$  and the navigation state  $\hat{x}$  is important. The navigation mechanization computes  $\hat{x}$  by integration of the IMU data between instants  $t_k$  and  $t_{k+1}$ , at which aiding measurements are available. At such instants,  $\hat{x}$  is used to predict the measurement  $\hat{y}_k^- = h(\hat{x}_k^-)$ . The filter uses the residual between the actual and predicted measurements to estimate  $\delta x^+$  in (25). When  $\delta x^+$  is available, the navigation state  $\hat{x}$  correction is

$$\hat{x}^+ = \hat{x}^- + \delta x^+. \quad (27)$$

After each navigation state correction by (27), the error state vector  $\delta x^+$  is zero since the navigation state estimate now incorporates this information. Clearly, if we correct  $\hat{x}$  immediately after each  $\delta x^+$  computation, this causes  $\delta x^+$  to be zero, and it is not necessary to propagate  $\delta x^-$  explicitly as in (20). Note that the error state vector contains  $\delta \rho$ , while the navigation state vector contains  $\hat{\Theta}$ . We cannot simply correct the attitude states of  $\hat{x}$ , as described in (27). Instead, we use  $\hat{\Theta}^-$  to correct transformation matrix  $\hat{R}_t^p$  via (13d), where

$$\hat{R}_t^p(\hat{\Theta}^+) = \hat{R}_t^p(\hat{\Theta}^-)(I - [\delta \rho \times]) \quad (28)$$

and then compute  $\hat{\Theta}^+$  from the resulting transformation matrix

$$\hat{\phi}^+ = \arctan2(\hat{R}_t^p[2, 3], \hat{R}_t^p[3, 3]) \quad (29a)$$

$$\hat{\theta}^+ = -\arctan\left(\frac{\hat{R}_t^p[1, 3]}{\sqrt{1 - (\hat{R}_t^p[1, 3])^2}}\right) \quad (29b)$$

$$\hat{\psi}^+ = \arctan2(\hat{R}_t^p[1, 2], \hat{R}_t^p[1, 1]) \quad (29c)$$

where  $\hat{R}_t^p[i, j]$  represents the  $(i, j)$  element of matrix  $\hat{R}_t^p(\hat{\Theta}^+)$  [4]. Function  $\arctan2(y, x)$  is the four-quadrant arc tangent function. To ensure numerical stability, it is necessary to normalize  $\hat{R}_t^p$  such that  $\det(\hat{R}_t^p) = 1$  before evaluating (29a)–(29c). The following sections describe the low-rate aiding sensors and their respective measurement correction. Measurement corrections require a measurement residual  $\delta y$ , sensor output matrix  $H$ , and measurement noise matrix  $R$  to evaluate (23) and (25).

1) *Attitude Update:* The attitude sensor consists of three magnetoresistive magnetic sensors, and a liquid filled two-axis tilt sensor. The raw measurements are normalized, linearized, and filtered internally to produce roll, pitch, and yaw information at 10 Hz. Due to the coupling with acceleration, the attitude measurement is only reliable when the acceleration is small. If raw magnetometer measurements are available, an alternate correction [4] eliminates this coupling. We also assume that the magnetometer is calibrated to compensate for hard iron characteristics of the operating region. Momentary magnetic spikes can easily be ignored using the measurement validation technique mentioned in Section III-F. The attitude sensor is disabled when the vehicle is operating near the ship hull.

The sensor model is

$$y_e = \Theta + n_e$$

where sensor noise  $n_e$  is distributed according to  $N(0, \text{diag}(\sigma_\phi^2, \sigma_\theta^2, \sigma_\psi^2))$  with  $\sigma_\phi \approx 0.02$  rad,  $\sigma_\theta \approx 0.02$  rad, and  $\sigma_\psi \approx 0.1$  rad. We can predict the measurement as

$$\hat{y}_e = \hat{\Theta}$$

and compute the measurement residual as

$$\delta y_e = y_e - \hat{y}_e \quad (30)$$

when a measurement arrives. To formulate the sensor output matrix  $H$  and measurement noise matrix  $R$ , a theoretical expression for the measurement residual in terms of the error state is necessary. In this case, an expression for  $\delta\Theta$  in terms of the  $\delta\rho$  portion of  $\delta x$  must be found. This formulation is similar to the relationship between the Euler attitude rates and platform angular rates that was derived in Section II. The quantity  $\delta\Theta$  describes attitude error relative to the intermediate rotation axes  $(\hat{i}_p, \hat{j}_2, \hat{k}_1)$ , while  $\delta\rho$  describes attitude error in tangent frame  $(\hat{i}_t, \hat{j}_t, \hat{k}_t)$ . Treating both  $\delta\Theta$  and  $\delta\rho$  as infinitesimal quantities

$$\delta\rho = R_1^t \delta\phi \hat{i}_p + R_2^t \delta\theta \hat{j}_2 + R_3^t \delta\psi \hat{k}_1 = \Sigma \delta\Theta$$

where

$$\Sigma = \begin{bmatrix} c\theta c\psi & -s\psi & 0 \\ c\theta s\psi & c\psi & 0 \\ -s\theta & 0 & 1 \end{bmatrix}.$$

Therefore, the theoretical measurement error expression is

$$\delta y_e = \{\Theta + n_e\} - \{\hat{\Theta}\} = \Sigma^{-1} \delta\rho + n_e = H\delta x + n_e$$

where the sensor output matrix is

$$H = [0 \quad \Sigma^{-1} \quad 0 \quad 0 \quad 0 \quad 0]. \quad (31)$$

Note that  $\Sigma^{-1}$  approaches a singularity as  $\theta \rightarrow \pm\pi/2$ , which is outside the sensor's measurement range. We assume that the vehicle will not operate near this singularity. The measurement noise matrix is

$$R = E\langle n_e n_e^T \rangle = \text{diag}(\sigma_\phi^2, \sigma_\theta^2, \sigma_\psi^2) \quad (32)$$

which is positive definite for all time. When an attitude measurement arrives, the Kalman filter evaluates (30)–(32) and then uses the results in (23)–(27) and (29a)–(29c) to correct the state estimate. Note that the Kalman filter formulation assumes that  $\delta\rho$  is small; therefore, the attitude sensor is used to initialize  $\hat{\Theta}$  at the start of the program. In Section IV-C, we show that attitude, in particular the yaw, is observable from the LBL system when the vehicle has a nonzero velocity; thus, the magnetic attitude sensor can be disabled after initialization.

2) *DVL Update:* The DVL measures velocity via the Doppler effect by first emitting encoded acoustic pulses from each of its four transducer heads. These pulses reflect off surfaces, such as the seafloor, and return back to each transducer. The instrument measures the change in frequency between the pulses emitted and those received, which relates to velocities along each beam direction relative to the reflecting object. The maximum update rate is approximately 7 Hz. To the authors' knowledge, all existing DVL aiding approaches, e.g., [8]–[10], utilize the three instrument frame velocities computed via a geometric transformation of the four beam measurements [7]. In certain situations, one or more beams may not return valid information. When fewer than three beams return valid information, the geometric transformation to relate beam velocities to instrument frame velocities cannot be computed; in such situations, an instrument frame velocity correction is not possible. It is possible to alleviate this restriction. To do so, we treat each beam velocity as a separate measurement. This approach does not require *bottom lock* and allows all available beam measurements to be used and validated independently. In addition, the measurement noise for each pair of beams is statistically independent, while the noise for the three instrument frame velocities is correlated, and the correlation matrix is not a standard DVL output. Let  $b = \{b_1, b_2, b_3, b_4\}$  be unit vectors along each beam direction. The  $i$ th Doppler measurement is

$$y_v = (v_{t/p}^p + \omega_{t/p}^p \times \ell_{D_i})b_i + n_v$$

which represents the instrument frame velocity along beam direction  $b_i$ . Vector  $\ell_{D_i}$  is the transducer head offset from the origin of the platform frame, and  $n_v$  is sensor noise with normal distribution  $N(0, \sigma_v^2)$  where  $\sigma_v \approx 0.021$  m/s. Therefore, the measurement estimate is

$$\hat{y}_v = (\hat{v}_{t/p}^p + \hat{\omega}_{t/p}^p \times \ell_{D_i})b_i$$

where  $\ell_{D_i}$  and  $b_i$  are known exactly, with residual

$$\begin{aligned}\delta y_v &= y_v - \hat{y}_v \\ &= \{(v_{t/p}^p + \omega_{t/p}^p \times \ell_{D_i})b_i + n_v\} - \{(\hat{v}_{t/p}^p + \hat{\omega}_{t/p}^p \times \ell_{D_i})b_i\} \\ &= b_i^\top \delta v_{t/p}^p + b_i^\top [\ell_{D_i} \times] \delta b_g + b_i^\top [\ell_{D_i} \times] n_g + n_v.\end{aligned}\quad (33)$$

The sensor output matrix is

$$H = \begin{bmatrix} 0 & 0 & b_i^\top & 0 & b_i^\top [\ell_{D_i} \times] & 0 \end{bmatrix} \quad (34)$$

and the measurement noise is

$$\begin{aligned}R &= E \left\{ \{b_i^\top [\ell_{D_i} \times] n_g + n_v\} \{b_i^\top [\ell_{D_i} \times] n_g + n_v\}^\top \right\} \\ &= b_i^\top [\ell_{D_i} \times] \sigma_g^2 I [\ell_{D_i} \times]^\top b_i + \sigma_v^2\end{aligned}\quad (35)$$

which is a positive scalar for all time. Note the significance of the sensor placement in relation to the gyro bias and gyro variance. Offset  $\ell_{D_i}$  affects observability to the gyro bias in (34), while  $\ell_{D_i}^2$  magnifies the effect of the gyro variance in (35). We ignore any correlation between the process noise  $n_g$  and measurement noise vectors. When a DVL beam measurement arrives, the Kalman filter evaluates (33)–(35) and then uses the results in (23)–(27) and (29a)–(29c) to correct the state estimate. Each beam provides a separate measurement correction.

3) *LBL Update*: The acoustic LBL system precisely measures the time of flight of sound waves propagating through water. The system consists of four remote baseline transponders and one transceiver that is fixed to the vehicle. At time  $t_0$  the vehicle transceiver generates a common interrogation ping. When each of the remote transponders detects the interrogation ping, they each wait a specified turnaround time, then respond. For example, transponder  $i \in \{1, 2, 3, 4\}$  responds  $250i$  ms after hearing the interrogation ping. The maximum travel time between any two transponders or between the vehicle and any one transponder is assumed to be less than 250 ms such that the turnaround time can identify the transponder. The vehicle receives the response from the  $i$ th transponder at time  $t_i$ . Fig. 4 illustrates the interrogation cycle. The total round-trip time for the  $i$ th transponder measurement is the sum of the travel time to the transponder plus the return travel time plus the turnaround time plus measurement error

$$y_{t_i} = \frac{1}{c(t_0)} \|B_i - P(t_0)\| + \frac{1}{c(t_i)} \|B_i - P(t_i)\| + T_i + n_t \quad (36)$$

where  $c(t)$  is the speed of sound in seawater and position vectors  $B_i$  and  $P(t)$  represent the position of transponder  $i$  and the vehicle transceiver at time  $t$ , respectively. The vehicle transceiver position in tangent frame is  $P = r_{t/p}^t + R_p^t \ell_L$ , where  $\ell_L$  is the sensor offset from the platform origin. Known constant  $T_i$  is the transponder turnaround time. Sensor noise  $n_t$  is distributed according to  $N(0, \sigma_t^2)$  where  $\sigma_t \approx 1.0$  ms. Note that under ideal conditions, the performance of this system is an order of magnitude better. However, the vehicle's thrusters and electrical system introduce additional uncharacterized noise. We assume the speed of sound is a slowly time-varying constant that is uniform throughout the operating region. If sound-speed information is available via measurement or *a priori* knowledge,  $c$  can

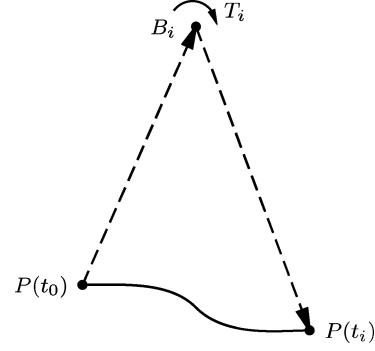


Fig. 4. LBL interrogation cycle. Dotted lines indicate the acoustic measurement. The solid line indicates an arbitrary vehicle trajectory.

be eliminated from the state vector. Therefore, the measurement estimate is

$$\hat{y}_{t_i} = \frac{1}{\hat{c}(t_0)} \|B_i - \hat{P}(t_0)\| + \frac{1}{\hat{c}(t_i)} \|B_i - \hat{P}(t_i)\| + T_i$$

where the transponder position  $B_i$  is known. The algorithm stores the current state estimate  $\hat{P}(t_0)$  at time  $t_0$ , then recalls it and  $\hat{P}(t_i)$  at  $t_i$  to compute measurement residual

$$\delta y_{t_i} = y_{t_i} - \hat{y}_{t_i}. \quad (37)$$

The delayed state dependence at  $t_0$  complicates the formulation of the measurement residual expression. One common technique to address this issue is to propagate the navigation state backwards in time [9], [11]–[13] using

$$\hat{P}(t_0) \approx \hat{P}(t_1) + \int_{t_1}^{t_0} \hat{\xi}(\tau) d\tau$$

where

$$\hat{\xi}(t) = \hat{R}_p^t (\hat{v}_{t/p}^p(t) + \hat{\omega}_{t/p}^p(t) \times \ell_L).$$

The navigation algorithm estimates the relative position between  $\hat{P}(t_0)$  and  $\hat{P}(t_i)$  by integrating the estimated transceiver velocity  $\hat{\xi}(t)$  from interrogation to reply. Another common technique is to treat the round-trip travel time as an average range [25]. The first approach does not account for the uncertainty in the vehicle trajectory over  $t \in [t_0, t_i]$ . The second approach is *ad hoc*. Neither approach accounts for the error state at  $t_0$ . Instead, we derive an approach that correctly accounts for the error state throughout the interrogation interval by using the known relationship  $\delta x(t_0) = \Phi(t_0, t_i) \delta x(t_i)$ . To formulate the measurement residual expression, we approximate nonlinear 2-norm expression  $d(t) = (1/c(t)) \|B_i - P(t)\|$  using a first-order Taylor series about state estimate  $\hat{x}$

$$\begin{aligned}d &= \hat{d} + \frac{\partial d}{\partial x} \Big|_{\hat{x}} (x - \hat{x}) + \frac{1}{2!} \frac{\partial^2 d}{(\partial x^2)} \Big|_{\hat{x}} (x - \hat{x})^2 + \dots \\ &\approx \hat{d} + \frac{\partial d}{\partial x} \Big|_{\hat{x}} \delta x.\end{aligned}$$

Define  $D(t) = \partial d / \partial x \Big|_{\hat{x}(t)}$ . The measurement residual is then

$$\delta y_t = \left\{ d(t_0) + d(t_i) + T_i + n_t \right\} - \left\{ \hat{d}(t_0) + \hat{d}(t_i) + T_i \right\}$$



$$\begin{aligned}
&= [d(t_0) - \hat{d}(t_0)] + [d(t_i) - \hat{d}(t_i)] + n_t \\
&\approx \left. \frac{\partial d(t_0)}{\partial x^\top} \right|_{\hat{x}(t_0)} \delta x(t_0) + \left. \frac{\partial d(t_i)}{\partial x^\top} \right|_{\hat{x}(t_i)} \delta x(t_i) + n_t \\
&= [D(t_0)\Phi(t_0, t_i) + D(t_i)] \delta x(t_i) + n_t
\end{aligned}$$

where the sensor output matrix is

$$H = D(t_0)\Phi(t_0, t_i) + D(t_i). \quad (38)$$

The state transition matrix  $\Phi(t_0, t_i)$  propagates the effect of the error state estimated at  $t_i$  backwards in time from time  $t_i$  to  $t_0$ . At each time step, from time  $t_0$  to  $t_i$ , the time propagation routine accumulates transition matrix  $\Phi(t_i, t_0)$  according to  $\Phi(t + \Delta t, t_0) = \Phi(t + \Delta t, t)\Phi(t, t_0)$ , where  $\Phi(t + \Delta t, t)$  is given in (19). When a measurement arrives, the measurement correction routine computes the inverse relationship, where  $\Phi(t_0, t_i) = \Phi^{-1}(t_i, t_0)$ , and applies the measurement correction. The nonzero partial derivative terms of matrix  $D(t)$  are

$$\begin{aligned}
\left. \frac{\partial d(t)}{\partial (r_{t/p}^t)^\top} \right|_{\hat{x}} &= -\frac{1}{\hat{c}(t)} \frac{(B_i - \hat{P}(t))^\top}{\|B_i - \hat{P}(t)\|} \\
\left. \frac{\partial d(t)}{\partial \rho^\top} \right|_{\hat{x}} &= \frac{1}{\hat{c}(t)} \frac{(B_i - \hat{P}(t))^\top}{\|B_i - \hat{P}(t)\|} [\hat{R}_p^t(t) \ell_L \times] \\
\left. \frac{\partial d(t)}{\partial c} \right|_{\hat{x}} &= -\frac{1}{\hat{c}^2(t)} \|B_i - \hat{P}(t)\|.
\end{aligned}$$

The measurement noise matrix is

$$R = E \langle n_t n_t^\top \rangle = \sigma_t^2 \quad (39)$$

which is a positive scalar for all time. When the vehicle transceiver emits a common interrogation ping at  $t_0$ , the correction routine stores the current state estimate  $\hat{x}(t_0)$ , while the time propagation routine begins accumulating the state transition matrix. During this time, the filter does not correct the navigation state according to (27) until the last transponder measurement arrives. This practice is necessary such that we can relate  $\delta x(t_i)$  to  $\delta x(t_0)$  via  $\Phi(t_0, t_i)$ . All intermediate corrections, including those from other aiding sensors, propagate  $\delta x^-$  through time. When an LBL measurement arrives, the Kalman filter evaluates (37)–(39) and then uses the results in (23)–(26) to correct the error state. When the last transponder measurement arrives, the filter corrects the navigation state according to (27) and (29a)–(29c). Timeout logic is necessary to handle the situation where the last measurement does not arrive. After all transponders reply or timeout, the cycle repeats.

For filter initialization, we set the diagonal elements relating to  $\delta r_{t/p}^t$  and  $\delta c$  of the initial covariance matrix  $P_0$  to be artificially small. This practice prevents large corrections to the navigation state during the first several LBL updates. If a sufficient number of transponder measurements are available, we initialize the navigation position to the trilateration result. No additional logic is necessary to encourage convergence.

4) *Pressure Update*: Over the vehicle's operating depths, the Saunders and Fofonoff (1976) relationship [26] between

pressure and depth is nearly linear, thus we model the pressure sensor as

$$y_z = s(r_{t/p}^t + R_p^t \ell_P) + b_z + n_z$$

where  $s$  and  $b_z$  scale and offset the pressure measurement, respectively, and  $s = [0, 0, s_z]$ . Vector  $\ell_P$  is the sensor position in platform frame. Sensor noise  $n_z$  is distributed according to  $N(0, \sigma_z^2)$  where  $\sigma_z \approx 194$  Pa. The measurement prediction is then

$$\hat{y}_z = s(\hat{r}_{t/p}^t + \hat{R}_p^t \ell_P) + b_z$$

where we assume that constants  $s_z$  and  $b_z$  are known. Therefore, the residual can be calculated as

$$\begin{aligned}
\delta y_z &= y_z - \hat{y}_z \\
&= \{s(r_{t/p}^t + R_p^t \ell_P) + b_z + n_z\} - \{s(\hat{r}_{t/p}^t + \hat{R}_p^t \ell_P) + b_z\} \\
&= s \delta r_{t/p}^t - s[\hat{R}_p^t \ell_P \times] \delta \rho + n_z.
\end{aligned} \quad (40)$$

The sensor output matrix is then

$$H = [s \quad -s[\hat{R}_p^t \ell_P \times] \quad 0 \quad 0 \quad 0 \quad 0] \quad (41)$$

with measurement noise

$$R = E \langle n_z n_z^\top \rangle = \sigma_z^2 \quad (42)$$

which is a positive scalar for all time. When a pressure measurement arrives, the Kalman filter evaluates (40)–(42) and then uses the results in (23)–(27) and (29a)–(29c) to correct the state estimate.

#### IV. ANALYSIS

To analyze our filter implementation, we examine the navigation state error, covariance, and measurement residuals. Here, we consider two scenarios in simulation and study the navigation state error and covariance. The navigation state error  $\delta x$ , which is only available when the true navigation state is available (i.e., in simulation), substantiates the filter's performance. The objective is to drive the navigation state error to zero. The covariance matrix quantifies the filter's expected size of  $\delta x \delta x^\top$ , where the square root of the diagonal describes the error state standard deviation. We expect the navigation state error to remain within three standard deviations of zero. To understand the behavior of the estimation performance, we perform observability analysis for scenarios when the acoustic sensors fail.

In Section V, we evaluate the measurement residuals for experimental data. The measurement residuals describe the performance of the filter's measurement predictions. These residuals should be white noise when the system and measurement models approximate the true system.

##### A. Observability

Observability analysis helps us determine if it is possible to estimate the error state  $\delta x$  from the output residuals  $\delta y$ . For simplicity, we address observability at one instant, rather than over a trajectory. Measurements are assumed to arrive simultaneously. Given system matrix  $F$  and a measurement output matrix  $H$ ,

we can compute observability matrix  $\mathcal{O}$  to determine the state subspace made observable via the measurement corrections associated with  $H$ . The observable and unobservable subspaces will be denoted by  $\Sigma_o$  and  $\Sigma_u$ , respectively. The portion of the state error within the unobservable subspace may remain constant or diverge, depending on the system characteristics. The rate of divergence deserves future discussion. To check observability, construct the observability matrix

$$\mathcal{O} = \begin{bmatrix} H \\ HF \\ \vdots \\ HF^{n-1} \end{bmatrix}$$

where matrix  $H$  is a measurement output matrix or combination of multiple measurement output matrices  $H = [H_1^\top, H_2^\top, \dots]^\top$ . The rank of  $\mathcal{O}$  is the dimension of observable subspace; if  $\mathcal{O}$  is full rank, we can estimate the entire error state from output  $y$  [27], [28]. The dimension of our system is 16, thus a rank of 16 is necessary to estimate  $\delta x$ . The rank of  $\mathcal{O}$  is complementary to the dimension of the unobservable subspace. Clearly,  $\mathcal{O}$  depends on  $x$  for nonlinear systems. We assume nominal conditions ( $\hat{x} = [0, 0, 0, 0, 0, 1500]^\top$ ) when computing  $\mathcal{O}$  unless stated. We also assume  $\omega_{i/e} \approx 0$  to eliminate the attitude observability gained from the rotation of the Earth.

### B. Simulation

The vehicle simulation is comprehensive. It models a 3-D environment, sensor performance, vehicle dynamics, and executes the actual vehicle software to approximate real-world performance. The sensor models are similar to those presented above, where in addition to measurement noise, we incorporate sporadic sensor dropouts and those due to poor geometry and loss of line of sight. Acoustic sensor models are simple. We do not attempt to model acoustic sound propagation or multipath effects, and we assume that acoustic transmissions are instantaneous with respect to the simulation step size (IMU rate). The vehicle model accounts for vehicle dynamics, hydrodynamics, currents, and thruster forces based on experimental data. For analysis purposes, we assume that this model represents the truth model.

The scenarios of interest are where different combinations of acoustic sensors drop out. These sensors, which include the LBL and DVL, are highly susceptible to interference, so it is important to examine the effect when their respective measurements are unavailable. For each scenario, the vehicle submerges to 5 m in depth, and then executes a lawnmower search pattern. The leg length is 40 m, with a row spacing of 5 m. After nine consecutive rows, the vehicle returns to the beginning of the first row and repeats the mission. The vehicle speed is 0.5 m/s. The acoustic baseline outlines a  $50 \times 50 \text{ m}^2$  box around the operating area. Fig. 5 illustrates the mission trajectory.

For each simulation, the true initial conditions are normally distributed about zero, except for the vehicle yaw angle and the speed of sound. Yaw is uniformly distributed about a circle, and speed of sound is normally distributed about 1450 m/s with variance  $(15 \text{ m/s})^2$ . All initial estimates are zero or the first available measurement, except for the speed of sound, which is 1500 m/s. For the nominal case, while the attitude sensor is being used, the

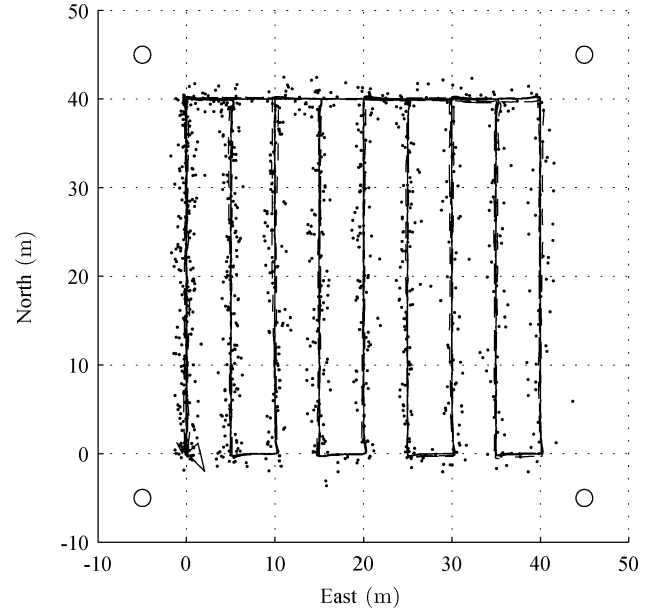


Fig. 5. North-east plot of one simulated mission from the incremental LBL dropout scenario, where the solid line represents the navigation estimate and the dashed line represents the true trajectory. The four circles represent the LBL transponders. For comparison, the small dots represent three- and four-range trilateration solutions when available.

system has full observability, thus we expect to estimate  $\delta x$ , and therefore,  $x$  when all sensors are functioning.

All results represent the *average* of 100 Monte Carlo simulations. That is to say, the  $\delta x$  signal represents the mean value of  $n = 100$  simulation samples, with the corresponding standard deviation estimate of  $\delta x$  scaled by  $\sqrt{1/n}$ . It is necessary to scale the standard deviation estimate as the averaging process decreases the signal's variation. All  $\delta x$  divergence rates indicated in each figure are for one standard deviation. The initial conditions for all simulations are randomized, as described above.

### C. Incremental LBL Dropouts, Limited Compass Aiding

First, consider the ship-hull inspection scenario. Operators place one LBL transponder at each corner of a ship and deploy an inspection vehicle. The vehicle executes several passes around and underneath the hull, searching for objects of interest. In this scenario, the keel frequently obstructs line of sight between the vehicle and one or more transponders, and, due to magnetic anomalies, vehicles typically operate without a magnetic compass. To illustrate the system performance in this scenario, we sequentially drop out LBL transponders. Transponder one fails at 600 s, followed by transponders two, three, and four at 1200, 1800, and 2400 s, respectively. Yaw aiding is only available during the first 30 s of the mission, which allows the algorithm to estimate  $\Theta$  such that  $\delta \rho$  becomes small before disabling the compass. The DVL, pressure, and inclinometers continue to aid the system. Figs. 6–8 illustrate the performance of the east position, azimuth, and speed of sound error states, respectively.

On interval  $t \in [30, 600] \text{ s}$ , where the vehicle is navigating the search pattern with four transponders and no compass, the system has full observability. If the vehicle's horizontal velocity and angular rate were zero, the system would have  $\text{rank}(\mathcal{O}) =$

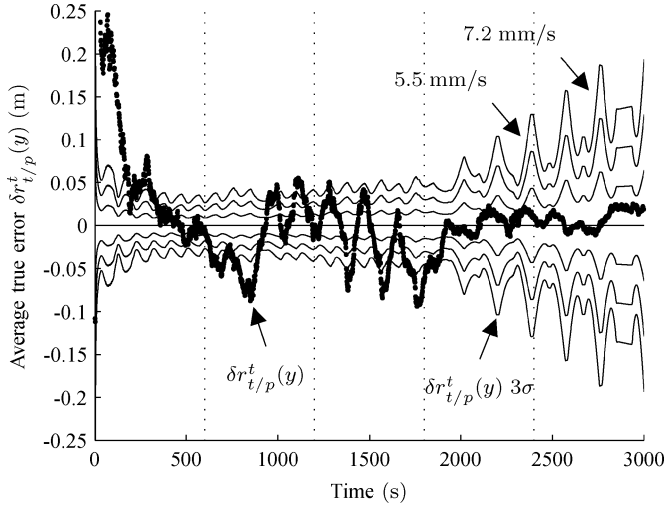


Fig. 6. East position error  $\delta r_{t/p}^t(y)$  for incremental LBL transponder dropouts and limited compass aiding. LBL transponders drop out at multiples of 600 s. The oscillations in standard deviation correlate to the vehicle trajectory and its relationship to each transponder.

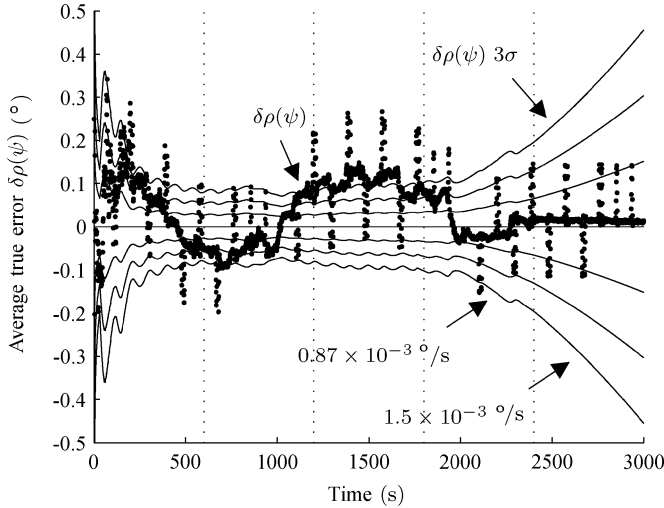


Fig. 7. Azimuth error  $\delta \rho(\psi)$  for incremental LBL transponder dropouts and limited compass aiding. LBL transponders drop out at multiples of 600 s. The true azimuth error is computed using (13a).

15. The unobservable subspace  $\Sigma_u$  then spans a linear combination of  $\{\delta r_{t/p}^t(x, y), \delta \rho(\psi)\}$ . This result is intuitive because the LBL transceiver remains stationary, and we cannot resolve azimuth from a single point in the horizontal plane. Observability analysis indicates that velocity in the horizontal direction promotes  $\mathcal{O}$  to full rank; vertical velocity does not. Vehicle rotation also promotes  $\mathcal{O}$  to full rank, where transceiver offset  $\ell_L \neq 0$ .

The loss of one transponder at  $t = 600$  s causes a subtle loss in observability. When transiting with nonzero horizontal velocity, the system has full observability as before. However, if the vehicle were to rotate in place with  $\psi \neq 0$ , linear combinations of  $\{\delta r_{t/p}^t(x, y), \delta \rho(\psi), \delta c\}$  would not be observable. When stationary, the system has  $\text{rank}(\mathcal{O}) = 15$ .

Losing of a second transponder at  $t = 1200$  s increases the dimension of  $\Sigma_u$  to 2 when stationary, where  $\Sigma_u$  spans linear combinations of  $\{\delta r_{t/p}^t(x, y), \delta \rho(\psi), \delta c\}$ . Velocity in the horizontal direction no longer achieves full observability. The algo-

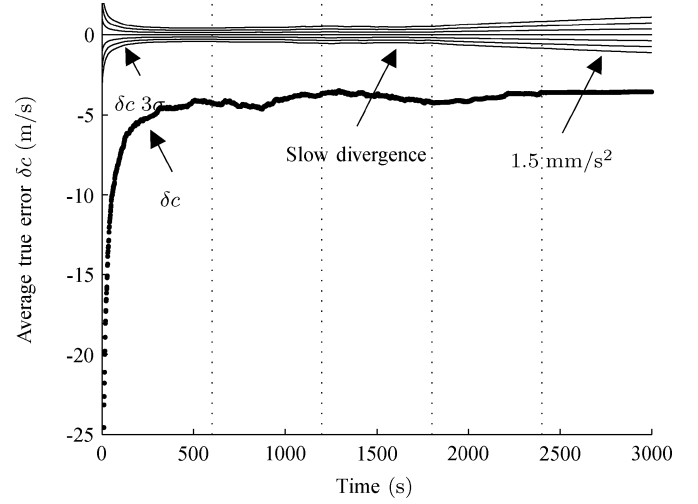


Fig. 8. Sound-speed error  $\delta c$  for incremental LBL transponder dropouts and limited compass aiding. LBL transponders drop out at multiples of 600 s.

rithm cannot differentiate between certain linear combinations of  $\delta r_{t/p}^t(x, y)$  and  $\delta c$ .

The loss of the third transponder at  $t = 1800$  s results in loss of observability that is exhibited by slow divergence of the position estimation error. Figs. 6 and 7 indicate the divergence rates for east position error and azimuth error, respectively. On interval  $t \in [1800, 2400]$  s, where only one transponder operates,  $\text{rank}(\mathcal{O}) = 13$  for zero velocity and  $\Sigma_u$  spans linear combinations of  $\{\delta r_{t/p}^t(x, y), \delta \rho(\psi), \delta c\}$ . For nonzero horizontal velocities,  $\text{rank}(\mathcal{O}) = 14$  and  $\Sigma_u$  spans linear combinations of  $\{\delta r_{t/p}^t(x, y), \delta c\}$ . Losing all transponders reduces observability to 11 states and  $\Sigma_u$  spans linear combinations of  $\{\delta r_{t/p}^t(x, y), \delta \rho(\psi)\}$ ,  $\{\delta b_g(\psi)\}$ , and  $\{\delta c\}$ . Note that as  $\|B_i - \hat{P}(t)\| \rightarrow 0$  in (38),  $\delta c$  becomes weakly observable. Thus, for small area searches such as the scenario presented here, the algorithm may be unable to estimate  $\delta c$  accurately as a result of the LBL sensor performance characteristics. We assume  $\sigma_t \approx 1.0$  ms (approximately 1.5 m/s) and  $\sigma_c \approx 0.1$  m/s. Fig. 8 shows that we cannot estimate the true speed of sound within 5 m/s for the given scenario.

#### D. Incremental DVL Beam Dropouts, No LBL Aiding

Consider the scenario when the LBL sensor is unavailable and the DVL begins to malfunction. Beam one fails at 200 s, followed by beams two, three, and four at 400, 600, and 800 s, respectively. The attitude and pressure sensors continue to aid the system. Figs. 9 and 10 depict the performance of velocity error  $\delta v_{t/p}^p(u)$  and accelerometer bias error  $\delta b_a(u)$ . Initially, the north and east error states, as well as the speed of sound, are not observable, and  $\text{rank}(\mathcal{O}) = 13$ . The unobservable subspace spans linear combinations of  $\{\delta r_{t/p}^t(x, y)\}$  and  $\{\delta c\}$ . This result is expected since no sensors aid position or speed of sound. When beam one fails, there is no additional loss in observability. Subspace  $\Sigma_u$  transforms, but the general relationships remain the same. Fig. 9 shows only a slight decrease in performance.

The performance resulting from the loss of a second beam depends on the particular beam lost. Our DVL points downward with each beam splayed outward at  $30^\circ$ , and  $90^\circ$  apart.

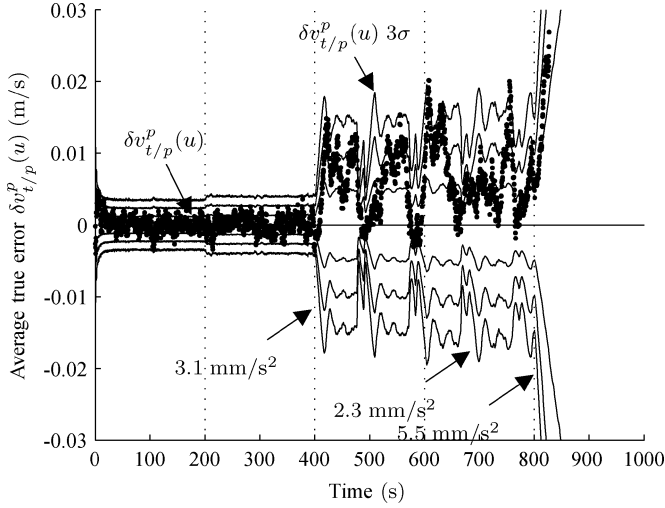


Fig. 9. Velocity error  $\delta v_{t/p}^p(u)$  for incremental DVL beam dropouts and no LBL aiding. DVL beams drop out at multiples of 200 s.

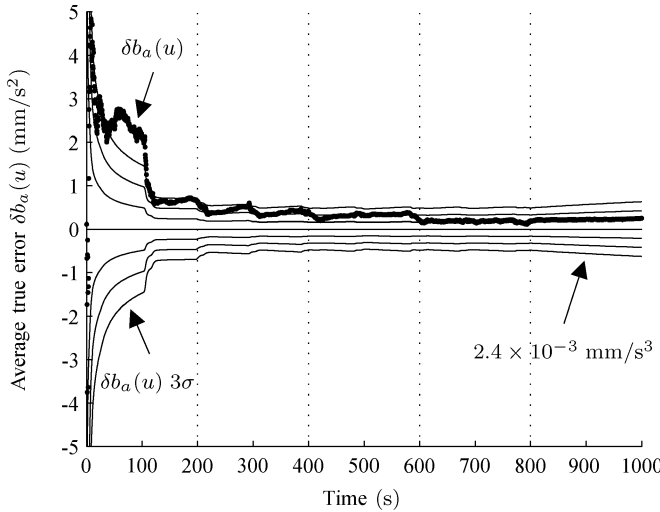


Fig. 10. Accelerometer bias error  $\delta b_a(u)$  for incremental DVL beam dropouts and no LBL aiding. DVL beams drop out at multiples of 200 s.

If two adjacent beams remain, the unobservable subspace remains the same dimension and the performance loss is subtle. If two opposing beams remain, the effect is detrimental. This result is due to the relationship between the sensor geometry and vertical axis. Since the pressure sensor provides information related to vertical velocity, it is desirable to measure other velocity components. Two opposing beams form a plane coincident with vertical axis, and thus no velocity information is available perpendicular to this plane. Our simulation reveals this condition, where the dimension of  $\Sigma_u$  increases to 5 and the rank of  $\mathcal{O}$  drops to 11. Linear combinations of  $\{\delta r_{t/p}^t(x, y), \delta v_{t/p}^p, \delta b_a\}$  and  $\{\delta c\}$  are not observable. From Fig. 9, we see that the observability is dependent on the system state. To understand this behavior better, we perform a separate observability analysis for different conditions.

For nonzero velocity, such as when the vehicle is tracking the segment between two waypoints,  $\Sigma_u$  has dimension 5. For nonzero angular rates, such as when the vehicle achieves a waypoint and maneuvers towards the next waypoint,  $\Sigma_u$  has

dimension 4. Linear combinations of  $\{\delta r_{t/p}^t(x, y), \delta v_{t/p}^p, \delta b_a\}$  and  $\{\delta c\}$  are not observable for both cases. Finally, when the vehicle has a nonzero roll or pitch angle,  $\Sigma_u$  has dimension 3. For this condition, the unobservable subspace is similar to a single beam failure. The oscillations in Fig. 9 correspond to the trajectory of the vehicle. At each waypoint, the vehicle maneuvers (with nonzero angular rates, and a slight roll angle) towards the next waypoint and the solution converges. When tracking the segment between two waypoints, the solution diverges. Losing a third beam is similar to the previous case, where the dimension of  $\Sigma_u$  is 5. The performance loss is subtle over interval  $t \in [600, 800]$  s. The divergence rates are comparable to a two-beam failure.

A total loss of the DVL causes divergence rates to increase. The divergence rate corresponding to velocity error  $\delta v_{t/p}^p(u)$  is  $5.5 \text{ mm/s}^2$  and to accelerometer bias error  $\delta b_a(u)$  is  $2.4 \times 10^{-3} \text{ mm/s}^3$ . The rank of  $\mathcal{O}$  drops to nine states, and the system can no longer maintain an acceptable level of performance. Note that this scenario illustrates the worst case. Intermittent beam dropouts result in only a slight decrease in performance due to an effective lower aiding rate.

## V. EXPERIMENTAL RESULTS

The following experimental results are from a demonstration at the 2007 Autonomous Underwater Vehicle Festival (AUVFest). The mission plan was to submerge to 3 m in depth for 2 min, then execute two sets of 3-D waypoints at 1 kn. The first series of waypoints consisted of vertically stacked legs between two waypoints. During this phase, i.e., for  $t \in [120, 740]$  s, the navigational goal was to observe the unknown parameters (yaw and biases) before proceeding to the second series of waypoints underneath a barge. The second series of waypoints, i.e., for  $t \in [740, 2500]$  s, consisted of a lawnmower search pattern in a continuous loop, similar to the scenario presented in Section IV. Due to severe magnetic interference from the barge, we chose to operate the vehicle without attitude aiding for  $t \in [120, 2500]$  s. The acoustic baseline outlines a  $36 \times 9 \text{ m}^2$  box around the second series of waypoints. Since the true state is not available, we present analysis of select error state covariances and measurement residuals. Note that the sensor data presented here is identical to that presented in [9]; however, here we reprocessed the raw data through the algorithms presented in this paper.

Position accuracy is a critical metric for inspection-class vehicles. This information allows operators to localize objects of interest, reacquire contacts, and navigate through complex environments. Fig. 11 illustrates the estimated standard deviation of the north, east, and down error states during the AUVFest demonstration. These results are consistent with the simulation results in Fig. 6. The convergence is dependent on the acoustic baseline geometry, vehicle trajectory, and several important factors. These factors include accuracy of the baseline calibration, the estimate of the speed of sound, and the estimate of the vehicle attitude.

We determine the acoustic baseline geometry before deployment via acoustic calibration. Using a spare transponder, the calibration algorithm measures round-trip travel times to each transponder and among all transponders. The algorithm assumes the relative layout of the transponders to formulate a geometric

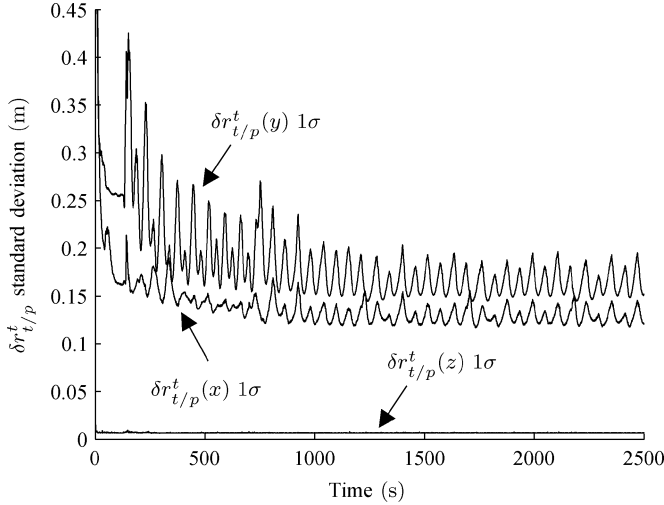


Fig. 11. North, east, and down position error  $\delta r_{t/p}^{t/p}$  standard deviation. The standard deviation estimate converges to 13, 17, and 0.7 cm for north, east, and down position errors, respectively. These results are subject to the baseline configuration and do not necessarily mean that  $\delta r_{t/p}^{t/p}$  is this accurate.

solution, which provides estimates for the transponder locations and the speed of sound. For our demonstration, it estimated a sound speed of 1491 m/s. The transponder locations are in a local coordinate system, where transponder 1 identifies the origin and the vector from transponder 1 to transponder 3 defines the  $y$ -axis. The  $z$ -axis is vertical and the  $x$ -axis completes the right-handed orthogonal frame of reference. We transform these coordinates into tangent plane coordinates for navigation. The current hardware implementation requires us to perform this procedure before operating the vehicle. It is not possible to estimate the baseline online with our current hardware. Clearly, a poor baseline calibration will degrade performance.

Analyzing the LBL round-trip measurement residuals provides insight into the baseline calibration. Fig. 12 represents the measurement residuals for transponder 1. Several features are apparent. First, the residuals do not resemble white noise. Second, approximately 7% of the data lies beyond three standard deviations of its expected value. We attribute these erroneous measurements to acoustic noise and multipath effects. Simple filtering techniques tend to produce inconsistent results due to the slow update rate and position uncertainty. Our current algorithm assumes all LBL measurements are valid. Another notable feature evident in the data is a  $\pm 2$ -ms oscillation. This oscillation is evident in all transponder residuals and is consistent with a poor baseline calibration in simulation. Simulation results confirm that misalignment of one transponder will hinder performance of the entire system. The oscillation correlates to the direction of the vehicle trajectory. Fig. 11 also shows an oscillatory pattern in the north and east error state standard deviations.

Inaccuracies in the speed of sound estimate can also cause oscillations in the round-trip measurement residuals. Fig. 13 illustrates the estimate of the speed of sound. The calibration routine estimated 1491 m/s. However, the navigation algorithm converged near 1420 m/s, which is unrealistic, given environmental

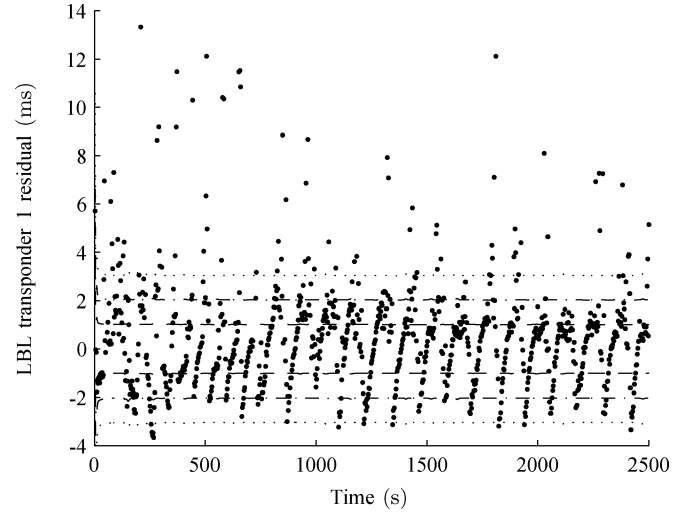


Fig. 12. LBL transponder 1 residual. This residual exhibits an oscillatory pattern that is consistent with baseline misalignment and the vehicle trajectory. All transponder residuals exhibit similar patterns. The horizontal lines indicate one, two, and three standard deviations about zero, where  $\sigma = \sqrt{HP - H^T + R}$ .

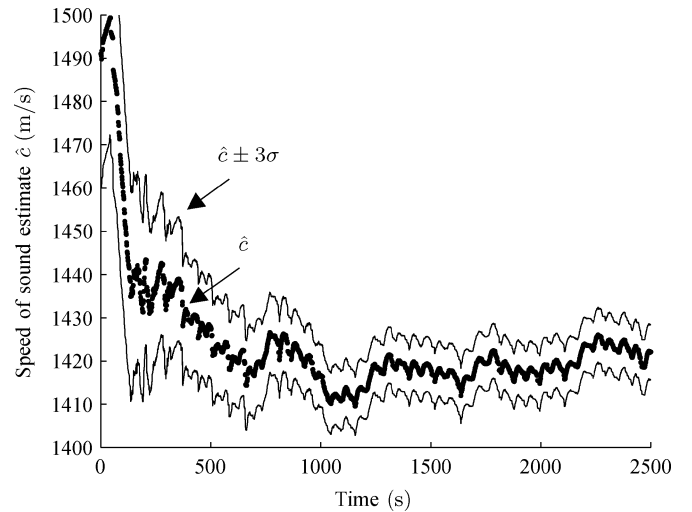


Fig. 13. Sound-speed estimate  $\hat{c}$ . Thin lines indicate three standard deviations beyond the estimate. The estimate converges to approximately 1420 m/s, which is suspicious, given the environmental factors.

conditions. Possible explanations include unknown biases, scale factors, and inaccuracies in the sensor clock frequency.

The azimuth error is of particular interest since yaw is an essential control signal and  $\delta\rho(\psi)$  is only observable via the LBL system. Poor estimation of error state  $\delta\rho(\psi)$ , and  $\delta\rho$ , generally, will result in inadequate navigation and control performance. Fig. 14 illustrates the azimuth and corresponding gyro bias error standard deviations. The azimuth error  $\delta\rho(\psi)$  standard deviation converges to  $0.5^\circ$ . This result does not necessarily mean that  $\tilde{\rho}(\psi)$  is this accurate; however, it is consistent with the simulation results in Fig. 7. These results were considered very good for our application.

Estimation of the unknown accelerometer and gyro bias vectors is a key aspect of our approach. Poor estimation of these parameters leads to inaccuracies in the time propagation of the navigation state vector, and thus poor measurement predictions

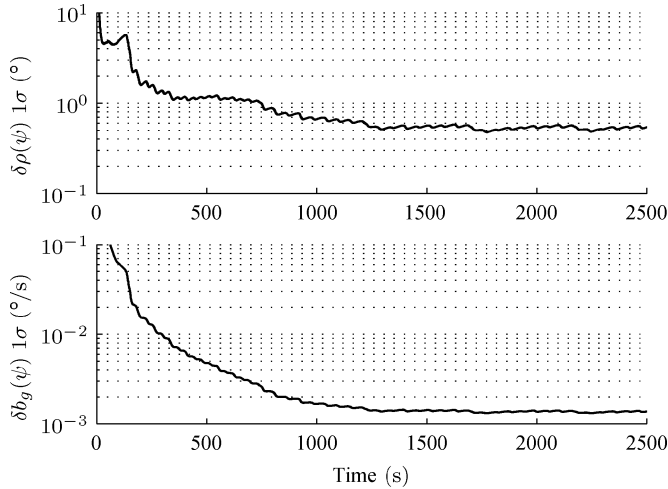


Fig. 14. Semilog plots of azimuth and gyro bias error standard deviations. Azimuth error  $\delta\rho(\psi)$  standard deviation converges to  $0.5^\circ$ . Gyro bias error  $\delta b_g(\psi)$  standard deviation converges to  $1.5 \times 10^{-3} \text{ }^\circ/\text{s}$ .

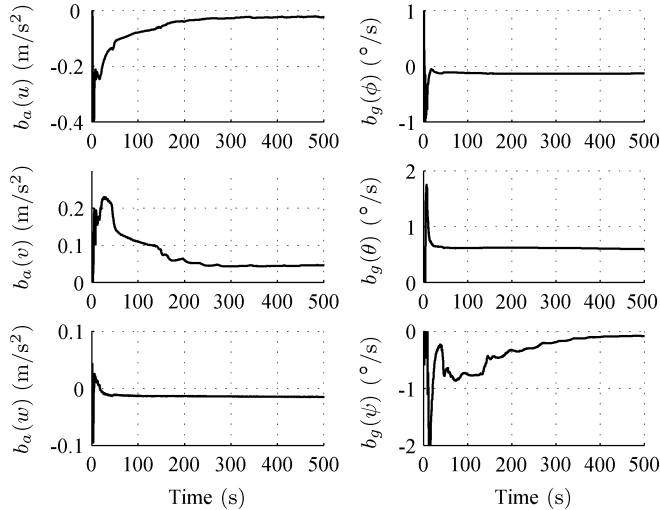


Fig. 15. Accelerometer and gyro bias estimates. Biases converge to reasonable values quickly.

for the aiding sensors. Fig. 15 illustrates the convergence of the unknown bias parameters. The forward and lateral gyro biases and vertical accelerometer bias converge rapidly to values that remain constant throughout the experiment. The convergence rate of the lateral accelerometer biases and the vertical gyro bias are dependent on the aiding sensors availability and the specific vehicle maneuvers which alter the structure of the observable subspace. All the bias estimates converge within 500 s and remain essentially constant thereafter.

Fig. 16 illustrates the measurement residuals for DVL beam 1. Initially, the residuals vary significantly as the estimates for platform velocity, attitude, and biases are converging. As the system calibration factors converge toward a quasi-steady state, the residuals resemble white noise. Residuals beyond three standard deviations are ignored.

We should note that the experimental results utilized the two-man portable Lockheed Martin/Perry Technologies CETUS-II vehicle as a platform of opportunity, where the

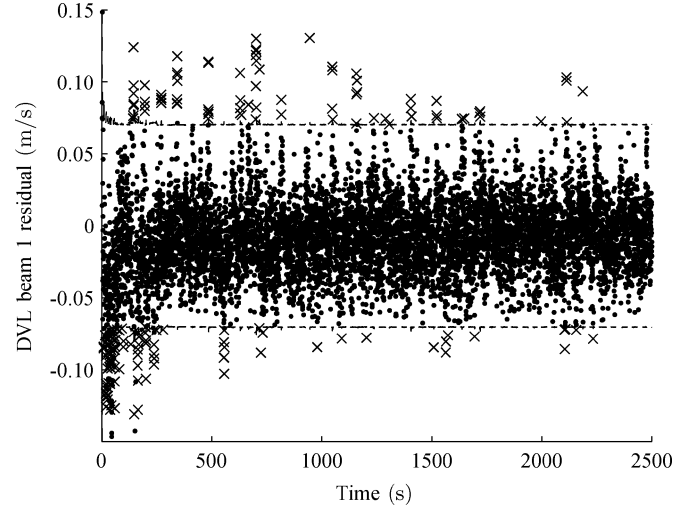


Fig. 16. DVL beam 1 residual. The dashed lines indicate three standard deviations, where  $\sigma = \sqrt{HP - H^T + R}$ . Residuals beyond three standard deviations are ignored as indicated by the  $\times$  marker.

authors replaced the original software. All software, including the vehicle navigation, guidance, and control algorithms, was written from scratch without reference to the original. Direct comparisons to the original platform are not available. All on-board sensors are original, except for modifications to the LBL firmware. Authors modified the stock Desert Star LBL firmware to provide interrogation and response timing feedback, rather than a trilaterization solution. This change allowed a tightly coupled LBL algorithm.

## VI. CONCLUSION

This paper presents an error state formulation of a navigation algorithm for an underwater vehicle. We derive the system kinematics model, then augment this model with unknown parameters from the sensor models to formulate the augmented system equations. Mechanization equations represent our estimate of the true augmented system equations, where the difference between the true and mechanization equations is the error state system. We design a Kalman filter to estimate this error state via measurement residuals from aiding sensors. The IMU propagates the navigation state, error state, and error state covariance through time, while aiding sensors provide corrections. Aiding sensors include an attitude sensor, DVL, LBL system, and a pressure sensor. Of particular interest are the measurement correction routines for the DVL and LBL system.

The DVL correction utilizes a tightly coupled approach to alleviate the need for bottom lock. When fewer than three beams respond, the filter can still incorporate valuable information. Simulation results and observability analysis show that incorporation of a single-beam measurement is far superior to a total dropout. Unaided inertial performance quickly degrades. A loosely coupled instrument frame approach would not be able to incorporate less than three beams, and thus would be equivalent to a total dropout. Further, individual beam corrections have statistically uncorrelated noise and permit individual beam validation. The result is a more robust system.

The LBL correction utilizes a tightly coupled approach that properly accounts for the error state throughout the measurement cycle via the state transition matrix. During the interrogation cycle, the navigation algorithm propagates error state separate from the navigation state. All measurement corrections, including those from other aiding sensors, accumulate into the error state. The navigation state continues to propagate via integration of the inertial measurements, but does not incorporate aiding measurement corrections until the completion of the LBL measurement cycle. The state transition matrix accumulates over the entire measurement cycle to relate the error state at interrogation to that at the final response. Alternate tightly coupled approaches ignore the error state, utilizing only the navigation state to account for the physical latencies in the measurement cycle. These approaches do not account for the uncertainty of vehicle trajectory between interrogation and reply, or the error state at interrogation.

Simulation and experimental results confirm our approach and implementation. Monte Carlo simulations of partial DVL and LBL acoustic failures indicate that partial failures have little or no effect on overall performance, provided that the vehicle continues to maneuver. Prolonged failure of multiple DVL beams or LBL transponders will degrade performance; however, the filter will continue to incorporate all available information. In effect, the system is robust to sporadic measurement failures. Experimental results at the 2007 AUVFest validate the simulation and system performance.

## REFERENCES

- [1] J. C. Kinsey, R. M. Eustice, and L. L. Whitcomb, "A survey of underwater vehicle navigation: Recent advances and new challenges," in *IFAC Conf. Manoeuver. Control Mar. Craft*, Lisbon, Portugal, Sep. 2006, CD-ROM.
- [2] J. J. Leonard, A. A. Bennett, C. M. Smith, and H. J. S. Feder, "Autonomous underwater vehicle navigation," MIT Mar. Robot. Lab., Cambridge, MA, Tech. Rep. 98-1, 1998.
- [3] R. G. Brown and P. Y. C. Hwang, *Introduction to Random Signals and Applied Kalman Filtering with Matlab Exercises and Solutions*, 3rd ed. New York: Wiley, 1996, ch. 5–7.
- [4] J. A. Farrell, *Aided Navigation: GPS with High Rate Sensors*. New York: McGraw-Hill, 2008, ch. 5 and 12.
- [5] A. Gelb, *Applied Optimal Estimation*. Cambridge, MA: MIT Press, 1974, ch. 3 and 4.
- [6] M. S. Grewal, L. R. Weill, and A. P. Andrews, *Global Positioning Systems, Inertial Navigation, and Integration*, 2nd ed. New York: Wiley, 2007, ch. 8.
- [7] RD Instruments, Inc., "ADCP coordinate transformation, formulas and calculations" San Diego, CA, P/N 951-6079-00, 1998.
- [8] L. Zhao and W. Gao, "The experimental study on GPS/INS/DVL integration for AUV," in *Proc. Position Location Navig. Symp.*, Apr. 26–29, 2004, pp. 337–340.
- [9] P. A. Miller, Y. Zhao, V. Djapic, and J. Farrell, "Autonomous underwater vehicle navigation," in *Proc. 15th Int. Symp. Unmanned Undersea Submersibles Technol.*, Durham, NH, Aug. 2007.
- [10] O. Hegrenæs, E. Berglund, and O. Hallingstad, "Model-aided inertial navigation for underwater vehicles," in *Proc. IEEE Int. Conf. Robot. Autom.*, May 19–23, 2008, pp. 1069–1076.
- [11] P. Baccou, B. Jouvencel, and V. Creuze, "Single beacon acoustic for AUV navigation," in *Proc. 10th Int. Conf. Adv. Robot.*, Aug. 22–25, 2001.
- [12] M. Morgado, P. Oliveira, C. Silvestre, and J. F. Vasconcelos, "USBL/INS tightly-coupled integration technique for underwater vehicles," in *Proc. 9th Int. Conf. Inf. Fusion*, Jul. 2006.
- [13] M. Morgado, P. Oliveira, C. Silvestre, and J. F. Vasconcelos, "Improving aiding techniques for USBL tightly-coupled inertial navigation system," in *Proc. IFAC 17th World Congr.*, Seoul, Korea, Jul. 6–11, 2008.
- [14] R. M. Rogers, *Applied Mathematics in Integrated Navigation Systems*, ser. Education. Reston, VA: AIAA, 2000, ch. 4.
- [15] H. Baruh, *Analytical Dynamics*. New York: McGraw-Hill, 1998, ch. 7.
- [16] M. D. Shuster, "A survey of attitude representations," *J. Astronaut. Sci.*, vol. 41, no. 4, pp. 439–517, Oct.-Dec. 1993.
- [17] J. Diebel, "Representing attitude: Euler angles, unit quaternions, and rotation vectors," Stanford Univ., Stanford, CA, Tech. Rep., 2006.
- [18] F. L. Markley, "Fast quaternion attitude estimation from two vector measurements," *J. Guid. Control Dyn.*, vol. 25, no. 2, pp. 411–414, 2002.
- [19] F. L. Markley, "Attitude error representations for Kalman filtering," *J. Guid. Control Dyn.*, vol. 26, no. 2, pp. 311–317, 2003.
- [20] K. R. Britting, *Inertial Navigation Systems Analysis*. New York: Wiley, 1972.
- [21] C. Moler and C. Van Loan, "Nineteen dubious ways to compute the exponential of a matrix," *SIAM Rev.*, vol. 20, no. 4, pp. 801–836, Oct. 1978.
- [22] J. D. Lambert, *Computational Methods in Ordinary Differential Equations*. New York: Wiley, 1973.
- [23] P. G. Savage, "Strapdown inertial navigation integration algorithm design part 1: Attitude algorithms," *J. Guid. Control Dyn.*, vol. 21, no. 1, pp. 19–28, Jan.-Feb. 1998.
- [24] P. G. Savage, "Strapdown inertial navigation integration algorithm design part 2: Velocity and position algorithms," *J. Guid. Control Dyn.*, vol. 21, no. 2, pp. 208–221, Mar.-Apr. 1998.
- [25] P. M. Lee, B. H. Jun, H. T. Choi, and S. W. Hong, "An integrated navigation systems for underwater vehicles based on inertial sensors and pseudo LBL acoustic transponders," in *Proc. MTS/IEEE OCEANS Conf.*, 2005, vol. 1, pp. 555–562.
- [26] P. M. Saunders and N. P. Fofonoff, "Conversion of pressure to depth in the ocean," *Deep-Sea Res.*, vol. 23, pp. 109–111, 1976.
- [27] W. L. Brogan, *Modern Control Theory*, 3rd ed. Upper Saddle River, NJ: Prentice-Hall, 1991, ch. 11.
- [28] C. Chen, *Linear System Theory and Design*, 3rd ed. New York: Oxford Univ. Press, 1998, ch. 6.



**Paul A. Miller** received the B.S. degree in mechanical engineering from Michigan Technology University, Houghton, in 2001 and the M.S. degree in mechanical engineering from University of Illinois at Urbana-Champaign, Urbana, in 2004, with an emphasis on nonlinear control of parallel mechanisms, robotics, and embedded systems.

At the Space and Naval Warfare (SPAWAR) Systems Center, San Diego, CA (2005–2009), he developed vehicle software architectures, sensor drives, guidance, navigation, and control algorithms for autonomous underwater vehicles in the Unmanned Maritime Vehicles Laboratory. His current focus is pedestrian navigation for first responders, first consulting for Acceleron Technologies, LLC, and then for Mine Safety Appliances (MSA), Cranberry Twp., PA (2008–2010). He continues his work with pedestrian navigation as a Principal Engineer at MSA.

Mr. Miller received a Department of the Navy Top Scientists and Engineers of the Year Award (2007) from the Assistant Secretary of the Navy, Research, Development, and Acquisitions, along with multiple letters of appreciation.



**Jay A. Farrell** (F'08) received the B.S. degrees in physics and electrical engineering from Iowa State University, Ames, in 1986 and the M.S. and Ph.D. degrees in electrical engineering from the University of Notre Dame, Notre Dame, IN, in 1988 and 1989, respectively.

At Charles Stark Draper Lab (1989–1994), he was a Principal Investigator on projects involving intelligent and learning control systems for autonomous vehicles. He is a Professor and former Chair of the Department of Electrical Engineering, University of California Riverside, Riverside. He is an author of over 160 technical publications. He is the author of the book *Aided Navigation: GPS With High Rate Sensors* (New York: McGraw-Hill, 2008). He is also coauthor of the books *The Global Positioning System and Inertial Navigation* (New York: McGraw-Hill, 1998) and *Adaptive Approximation Based Control: Unifying Neural, Fuzzy and Traditional Adaptive Approximation Approaches* (New York: Wiley, 2006).

Dr. Farrell received the Engineering Vice President's Best Technical Publication Award in 1990, and Recognition Awards for Outstanding Performance and Achievement in 1991 and 1993. He has served as Vice President Finance and Vice President of Technical Activities for the IEEE Control Systems Society (CSS). He is a distinguished member of the IEEE CSS.



**Yuanyuan Zhao** received the B.S. and M.S. degrees in electrical engineering from the University of Science and Technology, Beijing, China, in 1997 and 2000, respectively, and the Ph.D. degree in electrical engineering from the University of California Riverside, Riverside, in 2007.

Currently, she is with Servo Department, Western Digital Corporation, Lake Forest, CA. Her research interests are computational intelligence, learning control, nonlinear adaptive control, and nonlinear robust control.



**Vladimir Djapic** received the B.S. and M.S. degrees in electrical engineering from the University of California at San Diego, La Jolla, in 2000 and 2001, respectively, and the Ph.D. degree in electrical engineering from the University of California Riverside, Riverside, in 2009.

He joined NATO Undersea Research Centre (NURC), La Spezia, Italy, as a Scientist at the Systems Technology Department—The Autonomous Mine Countermeasures (AMCM) Program in 2008.

His research interests are in applying behavior-based, nonlinear, and adaptive algorithms to autonomous control of unmanned vehicles and testing them at sea. His previous employment was at the Unmanned Maritime Vehicle Laboratory (UMV), U.S. Navy Space and Naval Warfare Systems Center, San Diego, CA, where he had worked since 2002. His Office of Naval Research (ONR) funded work focused on utilizing advances in navigation, control, and sonar processing to exploit autonomous underwater vehicles (AUVs) for increasingly complex missions, a particular one being ship hull inspection. He participated in the design and implementation of sensor communications protocols for plug-and-play capabilities and adaptive, behavior-based mission planning on AUVs. He built a sensor package that was integrated onto the REMUS AUV. The objective of his research effort at NURC is to design a low-cost, but at the same time robust and effective mine neutralization system and perform multiple at-sea experiment.